# Evidence for the role of thermal and cloud merging in mesoscale convective organization

Sandrine Bony[1], Basile Poujol[1], Brett McKim[1], Nicolas Rochetin[2], Marie Lothon[3], Julia Windmiller[4], Nicolas Maury[1], Clarisse Dufaux[1], Louis Jaffeux[3], Patrick Chazette[5], and Julien Delanoë[6]

[1]LMD/IPSL, CNRS, Sorbonne University, Paris, France
[2]LMD/IPSL, Ecole Normale Supérieure, Paris, France
[3]LAERO, Université de Toulouse, CNRS, UT3, IRD, Toulouse, France
[4]Max Planck Institute for Meteorology, Hamburg, Germany
[5]LSCE/IPSL,CEA, Saclay, France
[6]LATMOS/IPSL, UVSQ Université Paris-Saclay, Sorbonne Université, CNRS, Guyancourt, France

**Correspondence:** Sandrine Bony (sandrine.bony@lmd.ipsl.fr)

**Abstract.** Observations from airborne field campaigns are used to study the interplay between boundary-layer thermals and clouds in the trades. The size distributions of thermal and cloud-base chords inferred from turbulence and horizontal lidar-radar measurements are robustly described by the sum of two exponentials. Analytical calculations and statistical simulations demonstrate that the two exponentials result from objects merging, respectively representing the populations of merged- and unmerged-object chords. They also show how circulations induced by convective objects facilitate the merging process. The observed day-to-day variability of these populations at cloud base can thus be tied to the variability of thermal merging across the depth of the subcloud layer. Clouds rooted in unmerged thermals are small and shallow while those rooted in merged thermals are wider and deeper. An intricate interplay between thermal- and cloud-merging arises: when thermal merging is weak, thermal number density is high and cloud bases merge easily, leading to strong mesoscale mass fluxes and "Gravel" shallow mesoscale organizations. In contrast, when thermal merging is strong, clouds are fed by sparser but wider thermals, leading to longer cloud lifetimes but weaker cloud merging, weaker mesoscale mass fluxes, and "Flower" mesoscale organizations. This interplay between thermal- and cloud-merging imposes an upper bound on cloud coverage and suggests a negative feedback on the growth of mesoscale circulations. Thermal merging also controls observed size distributions of thermals in deep convective regimes. The merging process thus appears to be a fundamental player in the mesoscale organization of convection.



## 1 Introduction

Moist convection generates a broad spectrum of cumulus clouds of varying widths, depths, and spacings. In regimes of shallow convection, this spectrum is dominated by two cloud types: very shallow clouds, whose tops do not exceed a few hundred meters above the cloud base, and deeper clouds, whose tops can reach several kilometres and often precipitate (Byers and Hall,

1955; Nuijens et al., 2014; Albright et al., 2023; Vial et al., 2023). By interacting with each other and with their environment, these clouds organize on the mesoscale (2 - 200 km, Agee (1987)). Deeper clouds, for instance, tend to be wider and more widely spaced than shallow clouds (Joseph and Cahalan, 1990) owing to their compensating subsidence, which inhibits the growth of nearby clouds (Bretherton, 1987). The development of deeper clouds is tied to the growth of shallow mesoscale circulations, which further reinforces their organization (Bretherton and Blossey, 2017; Narenpitak et al., 2021; Janssens et al., 2023). Taken together, this suggests a coordination between the emergence of different cloud types, cloud organizations, and mesoscale circulations.

Taking a bottom up view, convective cloud formation is rooted in coherent structures such as thermals that develop within the subcloud layer (LeMone and Pennell, 1976; Cohen and Craig, 2006; Seifert and Heus, 2013). The emergence of cloud types and organizations must therefore be related to changes in these structures. The natural place to study this interaction is at the intersection of the subcloud layer and cloud layer, i.e. at cloud base. The properties at cloud base are known to strongly control the fate of clouds. For instance, cloud widths at cloud base influence the turbulent entrainment at the edge of clouds (Blyth, 1993) and hence the cloud penetration depth (Malkus and Ronne, 1954; Simpson et al., 1965; Asai and Kasahara, 1967), and they are the primary modulator of the strength of convective mass fluxes (Böing et al., 2012; Dawe and Austin, 2012). These cloud widths are likely related to the sizes of thermals that permeate the subcloud layer, suggesting a coupling between thermal sizes, cloud types, cloud organizations, and mesoscale circulations.

Indeed, modeling studies have shown the interplay between thermal sizes, cloud base widths, and convective mass fluxes to play a major role in the transition between shallow and deep convection (Kuang and Bretherton, 2006; Khairoutdinov and Randall, 2006; Böing et al., 2012; Rochetin et al., 2014; Rousseau-Rizzi et al., 2017; Morrison et al., 2022), and it has long been recognized that cloud size distributions at the cloud base level are a fundamental variable to understand and represent cumulus convection (Simpson et al., 1965; Asai and Kasahara, 1967; Ooyama, 1971; Arakawa and Schubert, 1974; Craig and Cohen, 2006; Sakradzija et al., 2015; Neggers and Griewank, 2022). However, thermal and cloud base size distributions have largely been studied in large-eddy simulations and in ground-based observations over land (e.g. Neggers et al. (2003); Chandra et al. (2013); Lamer and Kollias (2015); Lareau et al. (2018); Öktem and Romps (2021)). Observations over the ocean are much more limited (López, 1977; LeMone and Zipser, 1980).

The wealth of observations collected during the EUREC$^4$A (*Elucidating the role of cloud-circulation coupling in climate*) airborne field campaign over the western tropical Atlantic (Bony et al., 2017; Stevens et al., 2021) present an opportunity to conduct such an investigation in the context of trade wind cumuli. The campaign provided observations of both clouds and their environment, including of the mesoscale circulations in which they were embedded ~~George et al. (2023)~~(George et al., 2023). More specifically, it characterized shallow convection for a month using a statistical sampling strategy in a region characterized by a large diversity and variability of mesoscale cloud patterns, the most prominent of which are commonly referred to as “Sugar”, “Gravel”, “Fish”, or “Flowers” (Stevens et al., 2020; Bony et al., 2020; Rasp et al., 2020; Janssens et al., 2021; Schulz, 2022). While the "Sugar" pattern consists exclusively of very shallow clouds, the other patterns are associated with a combination of shallow and deeper clouds in varying proportions and degrees of clustering (Mieslinger et al., 2019; Bony et al., 2020; Vial et al., 2021, 2023; Alinaghi et al., 2024).

In this study, we primarily use EUREC$^4$A observations (presented in section 2) to shed light on the interplay between thermals, clouds, mass fluxes and mesoscale circulations. First we characterize the size distributions of thermal chords (section 3) and cloud-base chords (section 4), and show that they can be described as a mixture of two chord populations and fitted by a sum of two exponentials. Section 5 uses an analytical framework, mathematical calculations and a simple statistical model to demonstrate that the double exponential size distributions can be physically interpreted as the result of the merging process. In section 6, we show how the length scales of cloud size distributions relate to those of thermals. Finally, we take advantage of the analytical framework, the statistical sampling of EUREC$^4$A and the large flight-to-flight variability of cloudiness, to further characterize the interplay between thermals and clouds, and explore its implications for convective mass fluxes and shallow mesoscale circulations, cloud mesoscale patterns and cloud fraction (Section 7). In section 8, we summarize our main findings, investigate their universality by using the first observations from ~~the MAESTRO (Mesoscale organisation of tropical convection) field campaign~~ a field campaign that took place in regimes of both shallow and deep convection, and discuss the perspectives of this study.

## 2 Airborne observations

The EUREC$^4$A field campaign (Bony et al., 2017; Stevens et al., 2021) took place in January-February 2020 in the North Atlantic trades, east of Barbados. In this study, we use observations from the SAFIRE ATR-42 (Bony et al., 2022) and from the HALO (Konow et al., 2021) research aircraft.

Over 4 weeks, the ATR conducted 18 research flights across 10 flight days, and spent most of its flight time near cloud base and within the subcloud layer. Each flight was 4.5 or 5 h long and followed a common flight pattern including typically two or three rectangles of about 120 km x 20 km flown around the cloud-base level (totaling 48 rectangles, i.e. about 36 hours of sampling) plus two L-shape patterns of about 120 km each flown within the subcloud layer. Most of the time, an additional leg of about 40 km long was flown about 60 m above the sea surface.

The aircraft measured turbulence (including horizontal and vertical velocity, inferred from the measurements of a five-hole nose radome) and humidity at a fast rate (25 Hz) using a Licor near-infrared gas analyzer and a KH20 hygrometer (Brilouet et al., 2021). At a flight speed of about 100 m.s$^{-1}$, this corresponds to an horizontal resolution of about 4 m. The humidity data used in the present analysis come from 30 km (5 min) stabilized flight segments (referred to as 'short segments'). They correspond to calibrated, detrended and high-pass filtered (at ~~1/6~~0.018 Hz) perturbations of water vapor mixing ratio (Brilouet et al., 2021). The payload also included a 355 nm backscatter lidar pointing horizontally through one of the aircraft windows (ALIAS, Chazette et al. (2020)) and a Doppler cloud radar (BASTA, Delanoë et al. (2016)) pointing horizontally through another window on the same side of the aircraft (Bony et al., 2022). This remote sensing allowed us to sample clouds horizontally over a much larger domain than in-situ measurements. The lidar could detect hydrometeors over a maximum range of 8 km, while the radar could detect non-drizzling clouds over a range of 3 to 6 km and drizzling clouds and rain up to 12 km. By combining horizontal radar-lidar measurements, we characterized the horizontal distribution of hydrometeors at a resolution of 25 m along the line of sight of both instruments (BASTALIAS dataset, Delanoë et al. (2021); Bony et al. (2022)).

During ATR flights, HALO was flying large circles of 200 km diameter at an altitude of 10 km, releasing dropsondes every 5 min (Konow et al., 2021). From these measurements, we inferred the subcloud layer height (Albright et al., 2022), the area-averaged cloud-base mass flux (Vogel et al., 2022) and, using the methodology proposed by Bony and Stevens (2019), the vertical profiles of area-averaged vertical velocity (George et al., 2021) and the strength of shallow mesoscale circulations (George et al., 2023). ~~We also use the multi-sensor cloud mask product derived from~~ From the multiple downward-looking instruments mounted on HALO (cloud radar, lidar and imagers)~~mounted on HALO (Konow et al., 2021).~~ , a multi-sensor cloud mask product was derived (Konow et al., 2021). We use the maximum cloud cover estimated on the basis of the 'most likely' and 'probably' cloud flags of each instrument.

At the end of this study, we also use the first airborne observations from the MAESTRO (*Mesoscale organisation of tropical convection*, https://maestro.aeris-data.fr/) field study that took place in August-September 2024 over the Eastern tropical Atlantic in the vicinity of Cape Verde. During this campaign, the SAFIRE ATR-42 aircraft sampled a wide diversity of convective regimes, ranging from shallow to deep convection. Its fast-rate humidity measurements (Jaffeux et al., submitted) allow us to characterize, as in EUREC$^4$A, the thermal chord length distributions at different vertical levels and to assess the universality of some of our findings across regions and convective regimes.

## 3 Convective thermals

In the trade-wind boundary-layer, water vapor is mixed vertically by turbulent eddies and discrete coherent structures, including moist, ascending anomalies which are called thermals. When the air parcels transported by the thermals reach the condensation level, they condense and form a cloud. We might thus expect the size characteristics of cloud bases to be related to the size of thermals permeating the subcloud layer.

To identify moist thermals from airborne measurements, we use the methodology proposed by Lenschow and Stephens (1980): segments of horizontal legs with humidity greater than half the standard deviation of humidity fluctuations for that leg, and larger than 25 m (i.e. 6 continuous data points), are defined as thermals. This detection is applied to all humidity fluctuations measured along 30-km segments (Brilouet et al., 2021) flown at different altitudes: near the sea surface (at a height of about 60 m, 11 flights), within the sub-cloud layer (in the middle of it – around 300 m ~~and~~ – and near the top of it – around 600 m, 16 flights) and ~~near~~ just above the cloud base level (between 600 and 800 m, 17 flights). Hereafter, for simplicity, the length of each thermal segment, or chord, will sometimes be referred to as 'thermal size'.

Statistics over the whole EUREC$^4$A campaign show that the mean thermal density (i.e. the number of intersected segments of thermals per horizontal distance flown by the aircraft) is largest near the surface (about 1.4 thermals km$^{-1}$) and smaller aloft, with about 1 thermal km$^{-1}$ in the middle of the subcloud-layer and near cloud base (Table 1). On the other hand, the mean size of thermals increases with height, varying from 93 m near the surface to about 200 m at the top of the subcloud layer. This can reflect the growth of individual thermals by entrainment or the coalescence of small thermals into larger ones as they rise and merge in the sub-cloud layer (section 5.2). Around the cloud base level, cloudy thermals (identified as those thermals in which every point in it has a relative humidity exceeding 98 %) represent about ~~19~~18% of the thermal population

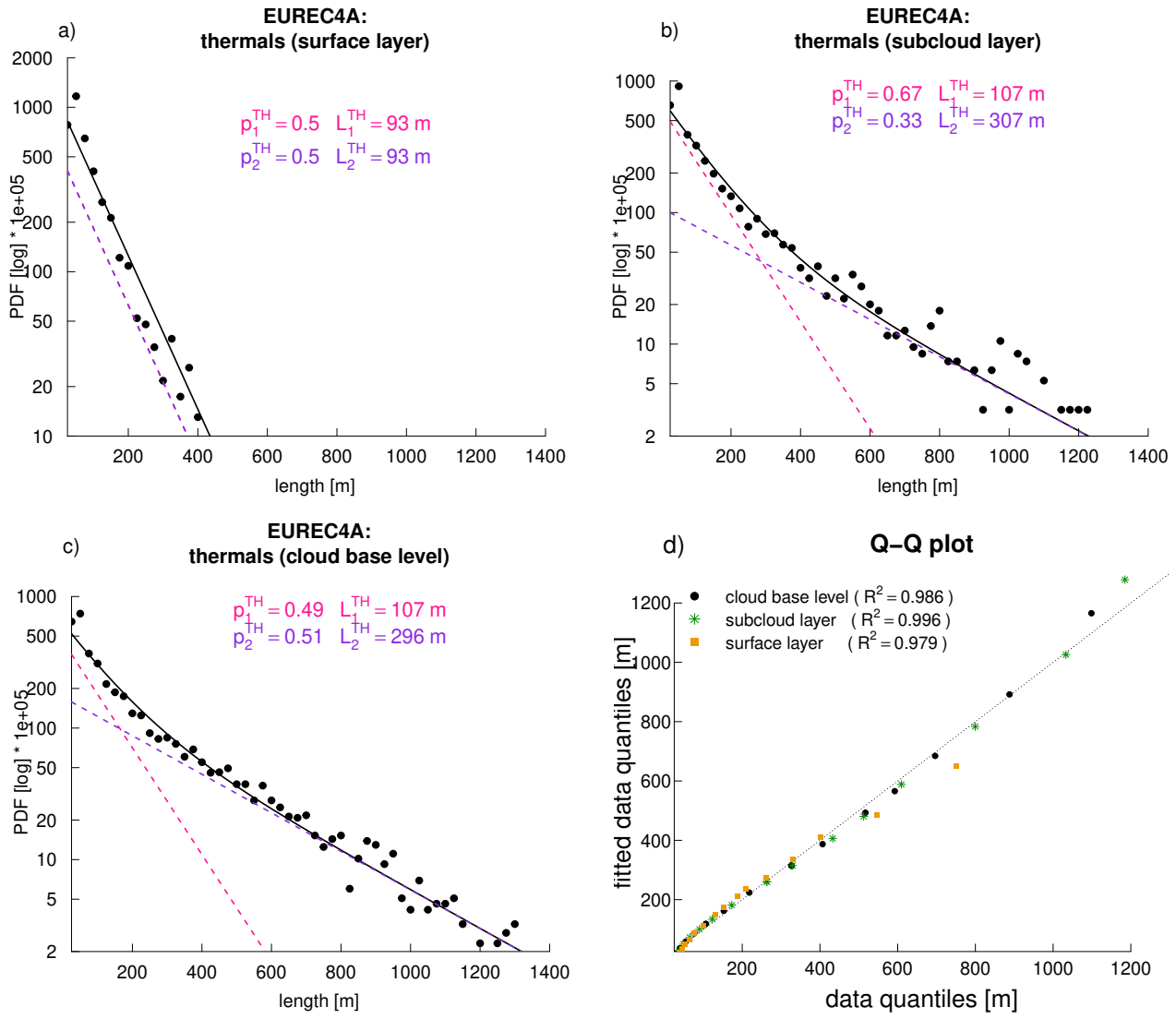


**Figure 1. Thermal size distributions:** Probability Distribution Function (PDF) of thermal chord lengths inferred from all EUREC$^4$A ATR turbulence measurements at different altitudes: (a) 60 m above the surface (b) within the sub-cloud layer (around 300 m or 600 m) and c) near cloud base (around 750 m). Also reported is the exponential fit (simple or mixture) and its parameters ($p_{1}^{thTH}$, $p_{2}^{thTH}$, $L_{1}^{thTH}$ and $L_{2}^{thTH}$, equation 1 – note that this fit is very similar to the one obtained using the mean fit parameters (averaged over all flights) reported in Table 1). (d) Comparison of the quantiles of the actual and fitted size distributions (Q-Q plot). Also reported are the $R^2$ coefficients (square of the Pearson correlation coefficients) of the linear regression for each flight level.

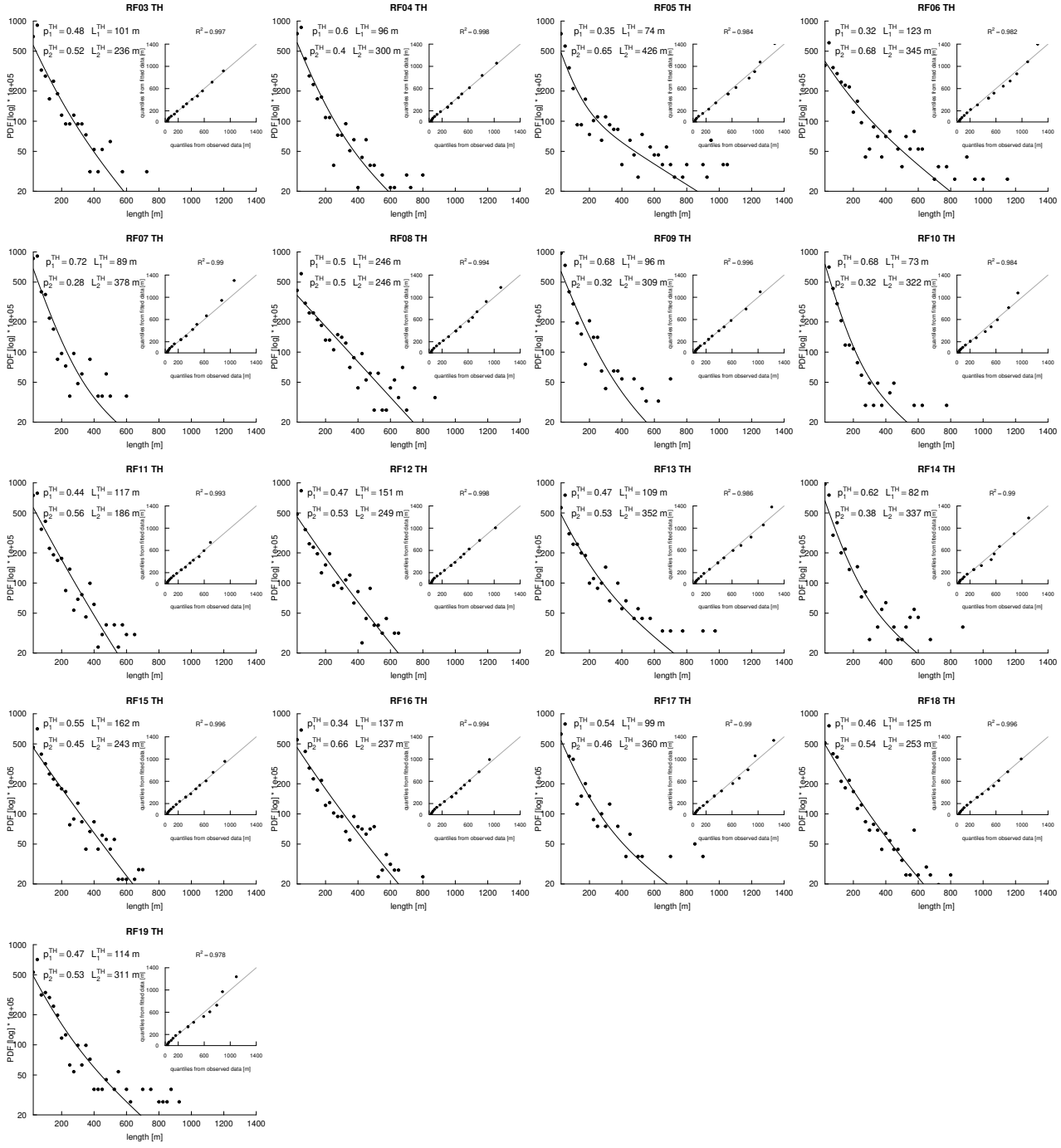


**Figure 2. Thermals from each EUREC$^4$A flight:** Probability distribution functions of the thermal chord lengths (in meters) derived for each ATR flight from turbulence measurements around the cloud base level (the distribution derived from all ATR flights together is shown on Fig. 1~~a~~c). Each panel shows the histogram, its fit by a sum of two exponentials (solid line) and the associated Q-Q plot (inset) to assess how well the ~~goodness~~ sum of ~~fit~~exponentials fits the data. The parameters of the fit ($p_1^{TH}$, $L_1^{TH}$, $p_2^{TH}$, $L_2^{TH}$) are also reported.

| Research | Date | Surface layer thermals | | | Subcloud layer thermals | | | | | | Cloud base thermals | | | | | |
|---|---|---|---|---|---|---|---|---|---|---|---|---|---|---|---|---|
| flight | MMDD | $\mathcal{D}^{TH}$ | $N^{TH}$ | $L_1^{TH}$ | $f^{TH}$ | $\mathcal{D}^{TH}$ | $N^{TH}$ | $p_1^{TH}$ | $L_1^{TH}$ | $L_2^{TH}$ | $f^{TH}$ | $\mathcal{D}^{TH}$ | $N^{TH}$ | $p_1^{TH}$ | $L_1^{TH}$ | $L_2^{TH}$ |
| RF03 | 0126 | 1.42 | 292 | 79 | 0.14 | 1.01 | 195 | 0.5 | 118 | 159 | 0.16 | 0.93 | 383 | 0.48 | 101 | 236 |
| RF04 | 0126 | 1.39 | 40 | 91 | 0.08 | 0.84 | 170 | 0.5 | 88 | 114 | 0.15 | 0.83 | 551 | 0.6 | 96 | 300 |
| RF05 | 0128 | - | - | - | 0.18 | 0.99 | 240 | 0.69 | 95 | 374 | 0.2 | 0.66 | 434 | 0.35 | 74 | 426 |
| RF06 | 0130 | 0.95 | 38 | 96 | 0.17 | 1.05 | 245 | 0.76 | 102 | 347 | 0.21 | 0.78 | 455 | 0.32 | 123 | 345 |
| RF07 | 0131 | - | - | - | 0.15 | 0.8 | 185 | 0.71 | 111 | 361 | 0.12 | 0.72 | 330 | 0.72 | 89 | 378 |
| RF08 | 0131 | - | - | - | 0.22 | 0.76 | 180 | 0.35 | 106 | 380 | 0.22 | 0.88 | 455 | 0.5 | 246 | 246 |
| RF09 | 0202 | - | - | - | 0.16 | 0.84 | 230 | 0.72 | 104 | 423 | 0.14 | 0.85 | 370 | 0.68 | 96 | 309 |
| RF10 | 0202 | 0.74 | 27 | 74 | 0.09 | 0.79 | 183 | 0.8 | 77 | 268 | 0.12 | 0.79 | 408 | 0.68 | 73 | 322 |
| RF11 | 0205 | 0.95 | 32 | 97 | 0.17 | 0.95 | 168 | 0.58 | 81 | 309 | 0.19 | 1.23 | 523 | 0.44 | 117 | 186 |
| RF12 | 0205 | 1.31 | 44 | 61 | 0.12 | 1.05 | 202 | 0.79 | 79 | 227 | 0.21 | 1.02 | 633 | 0.47 | 151 | 249 |
| RF13 | 0207 | 1.77 | 173 | 79 | 0.15 | 1.12 | 220 | 0.66 | 101 | 202 | 0.21 | 0.87 | 361 | 0.47 | 109 | 352 |
| RF14 | 0207 | - | - | - | 0.2 | 1.13 | 265 | 0.64 | 104 | 312 | 0.12 | 0.67 | 440 | 0.62 | 82 | 337 |
| RF15 | 0209 | 1.49 | 60 | 84 | 0.25 | 1.32 | 319 | 0.46 | 141 | 230 | 0.23 | 1.16 | 719 | 0.55 | 162 | 243 |
| RF16 | 0209 | 1.86 | 76 | 96 | - | - | - | - | - | - | 0.23 | 1.15 | 1018 | 0.34 | 137 | 237 |
| RF17 | 0211 | - | - | - | 0.24 | 1.31 | 343 | 0.43 | 113 | 242 | 0.22 | 0.98 | 319 | 0.54 | 99 | 360 |
| RF18 | 0211 | 1.74 | 67 | 127 | 0.26 | 1.37 | 312 | 0.48 | 145 | 229 | 0.24 | 1.25 | 813 | 0.46 | 125 | 253 |
| RF19 | 0213 | 1.73 | 72 | 139 | 0.29 | 1.43 | 331 | 0.52 | 136 | 278 | 0.22 | 1 | 445 | 0.47 | 114 | 311 |
| RF20 | 0213 | - | - | - | - | - | - | - | - | - | - | - | - | - | - | - |
| EUREC$^4$A mean | | 1.4 | 54 | 93 | 0.18 | 1.05 | 223 | 0.6 | 106 | 278 | 0.19 | 0.93 | 509 | 0.51 | 117 | 299 |
| | std | 0.38 | 75 | 23 | 0.06 | 0.22 | 82 | 0.14 | 21 | 86 | 0.04 | 0.19 | 189 | 0.12 | 41 | 63 |

**Table 1. Thermals observed during EUREC$^4$A in the surface layer, the subcloud layer and near cloud base:** For each ATR flight, $f^{TH}$ is the thermal coverage, $\mathcal{D}^{TH}$ is the thermal density (in $km^{-1}$), $N^{TH}$ is the number of chords, and $p_1^{TH}$ ($p_2^{TH}$ = 1 - $p_1^{TH}$), $L_1^{TH}$ and $L_2^{TH}$ (in meters) are the parameters of the double exponential fit (see equation 1). In the surface layer, the fit is close to a single exponential. Therefore, for the sake of space we report only $\mathcal{D}^{TH}$, $N^{TH}$ and $L_1^{TH}$. ~~Note that~~ The flights (or flight segments) without data are indicated by '-': no turbulence data are available for RF20 (failure of the inertial navigational system) and on the near-surface leg of RF14 (humidity measurements of bad quality). ~~The~~ , the near-surface was not sampled by the aircraft in RF05, RF07, RF08, RF09 and RF17, and the subcloud layer was not sampled during RF16.

at that level, and their size is on average slightly smaller than the mean size of moist thermals (~~158~~ 160 m vs ~~204~~200 m), which is consistent with ~~(Lenschow and Stephens, 1980)~~Lenschow and Stephens (1980).

However, at each altitude, the thermal dimensions exhibit a wide range of lengths. Near the surface, the length ranges from 25 m (the minimum size considered in our definition of thermals) to about 400 m, and the likelihood of finding a thermal of a given size decays exponentially with size (Fig. 1). At higher altitudes, the probability distribution function (PDF) of chord

| Research flight | Date MMDD | All clouds | | | | | | Non drizzling clouds | | | | | |
|---|---|---|---|---|---|---|---|---|---|---|---|---|---|
| | | $f^{CLD}$ | $N^{CLD}$ | $p_1^{CLD}$ | $L_1^{CLD}$ | $L_2^{CLD}$ | $R_f$ | $f^{CLD}$ | $N^{CLD}$ | $p_1^{CLD}$ | $L_1^{CLD}$ | $L_2^{CLD}$ | |
| RF03 | 0126 | 0.08 | 7203 | 0.81 | 210 | 831 | 2.2 | 0.04 | 5554 | 0.51 | 180 | 180 | |
| RF04 | 0126 | 0.03 | 5405 | 0.91 | 163 | 642 | 0.2 | 0.02 | 5224 | 0.5 | 156 | 156 | |
| RF05 | 0128 | 0.05 | 12348 | 0.5 | 139 | 139 | 0 | 0.05 | 12319 | 0.52 | 137 | 137 | |
| RF06 | 0130 | 0.04 | 10177 | 0.48 | 138 | 138 | 0 | 0.04 | 10124 | 0.48 | 136 | 136 | |
| RF07 | 0131 | 0.05 | 5031 | 0.76 | 178 | 678 | 1.3 | 0.03 | 3707 | 0.5 | 151 | 151 | |
| RF08 | 0131 | 0.04 | 5335 | 0.9 | 113 | 502 | 0.6 | 0.02 | 4767 | 0.51 | 102 | 102 | |
| RF09 | 0202 | 0.01 | 692 | 0.5 | 143 | 143 | 0 | 0.01 | 671 | 0.5 | 141 | 141 | |
| RF10 | 0202 | 0.03 | 2624 | 0.88 | 173 | 746 | 0.2 | 0.02 | 2316 | 0.51 | 149 | 149 | |
| RF11 | 0205 | 0.08 | 7779 | 0.86 | 157 | 913 | 0.2 | 0.06 | 7283 | 0.5 | 155 | 155 | |
| RF12 | 0205 | 0.06 | 7834 | 0.49 | 134 | 134 | 0 | 0.06 | 7781 | 0.46 | 130 | 130 | |
| RF13 | 0207 | 0.03 | 3687 | 0.99 | 185 | 657 | 0 | 0.03 | 3461 | 0.5 | 166 | 166 | |
| RF14 | 0207 | 0.02 | 2661 | 0.96 | 180 | 716 | 0 | 0.01 | 2538 | 0.5 | 165 | 165 | |
| RF15 | 0209 | 0.06 | 7997 | 0.48 | 142 | 142 | 0.1 | 0.05 | 7842 | 0.49 | 135 | 135 | |
| RF16 | 0209 | 0.07 | 7849 | 0.91 | 126 | 777 | 0.8 | 0.05 | 7072 | 0.47 | 115 | 115 | |
| RF17 | 0211 | 0.13 | 7922 | 0.58 | 178 | 795 | 9.8 | 0.04 | 4664 | 0.94 | 154 | 424 | |
| RF18 | 0211 | 0.1 | 7657 | 0.81 | 152 | 751 | 9.3 | 0.05 | 5797 | 0.5 | 140 | 140 | |
| RF19 | 0213 | 0.08 | 6972 | 0.7 | 178 | 857 | 1.3 | 0.05 | 5974 | 0.52 | 166 | 166 | |
| RF20 | 0213 | 0.03 | 2818 | 0.89 | 174 | 748 | 0.6 | 0.02 | 2056 | 0.51 | 141 | 141 | |
| 1 cloud | mean | 0.04 | 7810 | 0.49 | 139 | 139 | 0 | 0.04 | 5558 | 0.5 | 145 | 145 | |
| population | std | 0.02 | 4385 | 0.01 | 4 | 4 | 0 | 0.02 | 3026 | 0.02 | 19 | 19 | |
| 2 cloud | mean | 0.06 | 5611 | 0.84 | 167 | 740 | 2 | 0.04 | 4664 | 0.94 | 154 | 424 | |
| populations | std | 0.03 | 2106 | 0.11 | 25 | 106 | 3.4 | - | - | - | - | - | |

**Table 2. Cloud chords measured during EUREC$^4$A near cloud base:** For each ATR flight, $f^{CLD}$ is the cloud fraction, $N^{CLD}$ is the number of chords, and $p_1^{CLD}$ ($p_2^{CLD}$ = 1 - $p_1^{CLD}$), $L_1^{CLD}$ and $L_2^{CLD}$ (in meters) are the parameters of the bi-exponential fit (see equation 1). Note that $L_1^{CLD} \approx L_2^{CLD}$ ~~or $p_1^{CLD} \approx 1$~~ corresponds to a single exponential. Also reported is the rain fraction during each flight ($R_f$, in %).

lengths $P(x)$ is well fitted[1] by a mixture of two exponential functions ~~in proportions~~ with relative weights $p_1$ and $p_2 = 1 - p_1$, and characterized by length scales $L_1$ and $L_2$ (Rochetin et al., 2014), such as :

$$P(x) = \frac{p_1}{L_1} e^{-\frac{x}{L_1}} + \frac{p_2}{L_2} e^{-\frac{x}{L_2}}. \quad (1)$$

This suggests that the thermal chord ensemble is well described by a mixture of two thermal populations, of mean sizes ~~$L_1^{TH}$~~ $L_1^{TH}$ (about 100 m) and ~~$L_2^{TH}$~~ $L_2^{TH}$ (about 300 m)~~and in relative proportions $p_1^{TH}$ and $p_2^{TH}$, with $p_2^{TH}$ increasing with height~~

[1]The distributions are fitted using the R-package *MixtureInf* developed by Li et al. (2016), which is based on a penalized maximum likelihood estimate, or PMLE, approach~~.~~, with a penalty parameter $\lambda = 1$.

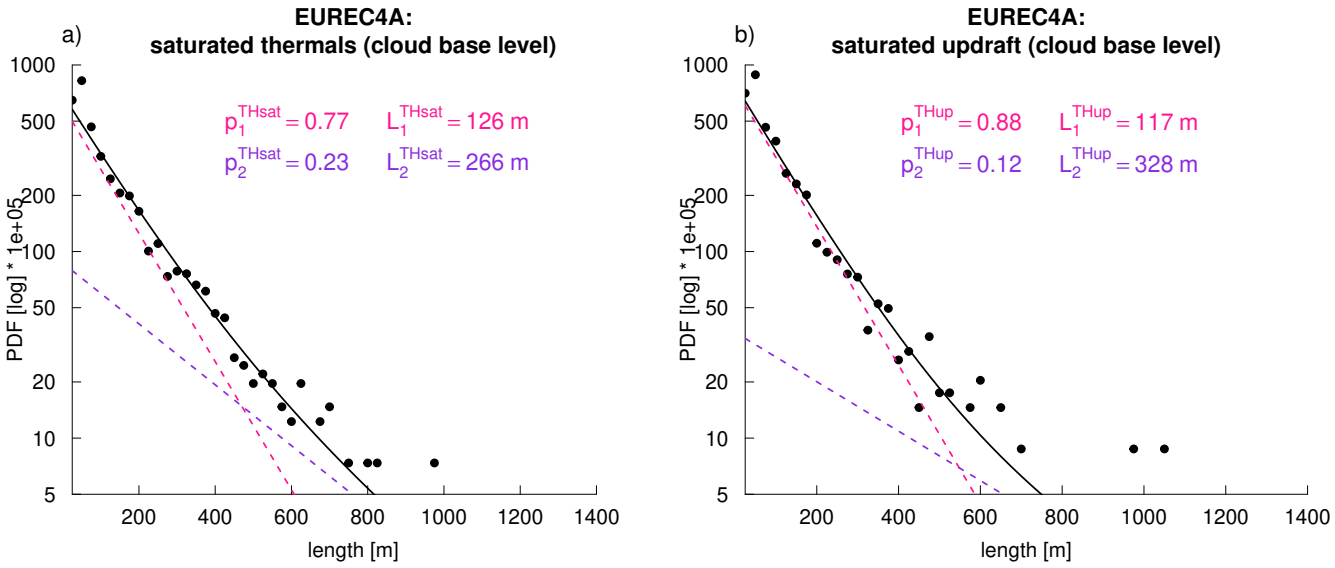


**Figure 3.** Probability distribution function of (left) cloudy thermal lengths and (right) cloudy updraft lengths measured by the ATR near the cloud-base level. Cloudy thermals are defined as moist thermals (or segments) whose points are saturated near the cloud base level (relative humidity exceeding 0.98), and cloudy updrafts are defined as cloudy thermals whose points all have a positive vertical velocity near cloud base).

~~at the expense of $p_1^{TH}$.This~~ . The comparison of the quantiles associated with the actual and fitted size distributions (so-called Q-Q plots shown on Fig. 1d and Fig. 2 ) confirms that this description is not only valid when considering all EUREC$^4$A data but also robust at the scale of individual flights~~(Fig. 2)~~, though the relative ~~proportion~~ weight and mean size of each population vary across flights (Table 1). Following these notations, the mean size of thermal chords is given by $L = p_1 L_1 + p_2 L_2$. Moreover, if N is the total number of thermal chords intersected by the aircraft along a horizontal distance of $\mathcal{L}$, the mean thermal density for this distance is given by $N/\mathcal{L}$.

~~Note that a mixture of two populations is still found near cloud base when considering only cloudy thermals (i. e. , moist thermals that are saturated at their top) or thermal updrafts (defined as moist thermalswhose points are all associated with both saturation and a~~ Thermals that overshoot the lifting condensation level (LCL) generate saturated thermal chords, or 'cloudy thermals'. The majority of these (84 % in the EUREC$^4$A data) are characterized by a mean positive vertical velocity ~~,~~ ('cloudy updrafts'). They may therefore be regarded as 'cloud shoots', i.e. incipient cloud bases formed immediately after thermals overshoot the LCL, that can subsequently grow into convective clouds rooted in boundary layer thermals. Fig. 3 ~~). The~~ shows that their size distribution is also well fitted by a mixture of two populations, and that their length scales $L_1^{TH}$ ~~and $L_2^{TH}$ of these particular thermals~~ $L_1^{THsat}$ and $L_2^{THsat}$ for cloudy thermals, and $L_1^{THup}$ and $L_2^{THup}$ for cloudy updrafts, are comparable to those ~~obtained when considering all moist thermals~~ of the whole thermal population (Fig. 1c)~~, but the number~~ . Flight-to-flight variations in the density of cloudy thermals ~~or thermal updrafts is much lower than the total number of moist thermals at the~~

~~same level (they represent only 19% and 16%~~($\mathcal{D}^{THsat}$) and cloudy updrafts ($\mathcal{D}^{THup}$) are strongly correlated with each other ($R^2$ = 0.96), and also with the total density of thermals $\mathcal{D}^{TH}$ ($R^2$ = 0.74 and 0.70, respectively, ~~of all moist thermals). Therefore,~~ Fig. S5). On average, however, $\mathcal{D}^{THsat}$ and $\mathcal{D}^{THup}$ are five to six times smaller than $\mathcal{D}^{TH}$, with a mean ratio $\mathcal{D}^{THsat}/\mathcal{D}^{TH}$ = 0.18 and $\mathcal{D}^{THup}/\mathcal{D}^{TH}$ = 0.15 in the EUREC$^4$A dataset. Therefore, to increase the statistical robustness of our investigations, in the following sections of this study we will ~~consider~~ analyze the flight-to-flight variations in thermal populations and size distributions by considering all moist thermals~~to increase the statistical robustness of our investigations~~.

## 4 Cloud-base widths

EUREC$^4$A pioneered the sampling of clouds through horizontal remote sensing thanks to sidewards-looking radar and lidar measurements across the ATR windows (Bony et al., 2022). Using the hydrometeors classification derived from the synergy of the lidar-radar remote sensing over a range of several kilometers away from the aircraft (Delanoë et al., 2021; Bony et al., 2022), we detect the length of cloud segments, or chords, along the line of sight of the lidar-radar measurements, perpendicular to the aircraft trajectory. The horizontal resolution of the hydrometeors classification along the line of sight of the radar and lidar is 25 m. A segment (or chord) corresponds to at least 2 continuous points associated with cloud or drizzle, i. e. reflectivities lower than 0 dBZ (drizzle is considered because the distinction between clouds and drizzle using radar reflectivity is ambiguous, and because drizzle falls within cloud base in the case of shallow cumuli). Horizontal remote sensing makes it possible to characterize the size distribution of cloud chords (hereafter referred to as 'cloud-base widths') through the sampling of one or multiple chords within each cloud, without having to determine whether chords sampled at different times belong to the same cloud or not. This allows us to characterize the irregular and complex shapes of cloud bases without making assumptions about cloud shapes, and to sample the cloud field around the cloud base level with much better horizontal sampling than would be possible with in-situ measurements along the aircraft's trajectory.

The cloud chord length distribution computed over the whole EUREC$^4$A campaign shows the presence of many small chords and fewer larger chords (Fig. 4a). As for thermals, the distribution is well fitted by a mixture of two populations ~~in proportions~~ with $p_1^{CLD}$ = ~~89 %~~ 0.9 and $p_2^{CLD}$ = 1 - $p_1^{CLD}$ = ~~11 %~~0.1. Each population is characterized by an exponential length distribution, with a scaling parameter corresponding to the average length of the chords in that population: $L_1^{CLD}$ = 156 m, and $L_2^{CLD}$ = 835 m.

However, the comparison of the different flights reveals that as for thermals, the cloud chord distribution varies strongly from flight to flight. Fig. 5 shows that for each individual flight, the distribution is still robustly fitted by a mixture of exponential distributions, but in variable proportions and with scaling parameters $L_1^{CLD}$ and $L_2^{CLD}$ that can vary ~~by ± 15%~~ significanly across flights (Table 2).

The variability of the cloud chord distributions around cloud base correlates with a number of cloud properties. Firstly, the clouds encountered on flights with only one cloud population (5 out of 18) are devoid of drizzle~~(Fig. 4b)~~, and for each flight, the PDF of cloud chords devoid of drizzle is well fitted by a single exponential (Fig. 4~~c-d~~b, Fig. S3 of Supplementary information). Since drizzle starts when the cloud depth exceeds about 2 km (Byers and Hall, 1955; Rauber et al., 2007), it suggests that the

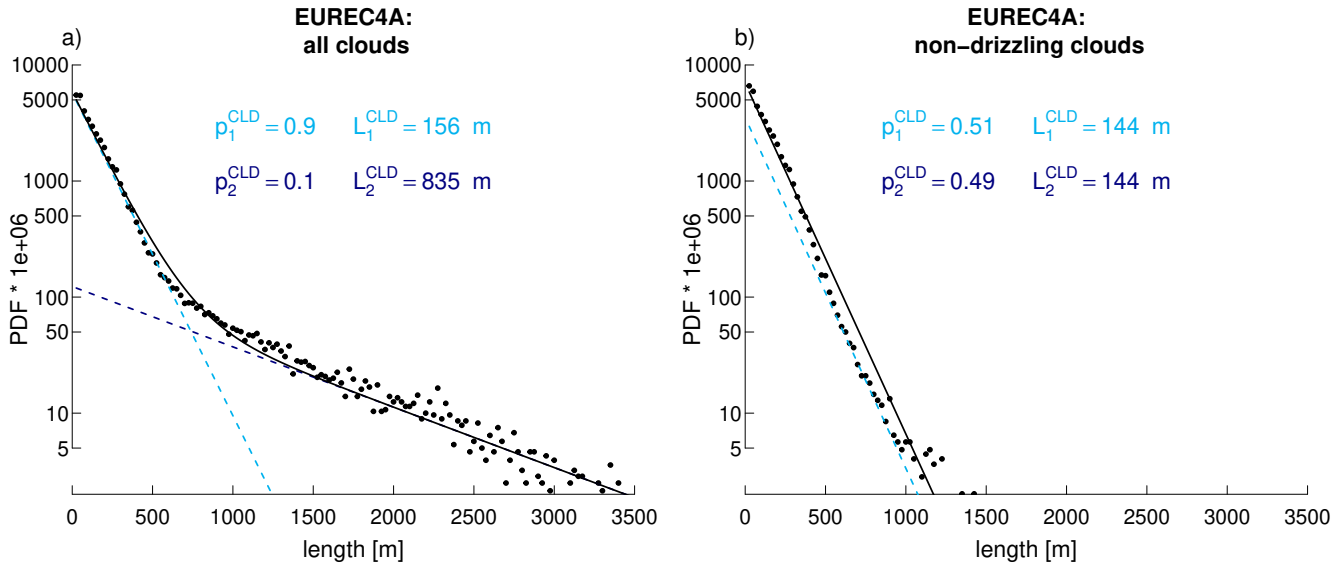


**Figure 4. Cloud chord length distributions derived from horizontal radar-lidar measurements around cloud base:** (a) PDF obtained by considering all EUREC$^4$A flights together fitted by a mixture of two exponential distributions (equation 1). (b) Same as (a) but for ~~individual ATR flights (flights in purple are those for which the chord length distribution is fitted by a single exponential). (c) and (d) Same as (a) and (b) but for~~ cloud chords devoid of drizzle. The parameters reported on each panel are those associated with each fit.

first cloud mode is associated with very low cloud tops, while the second mode includes cloud chords which are not only larger but also associated with deeper cloud tops than those of the first population.

These observations suggest that the two shallow cloud populations (very shallow and deeper) reported in previous studies (i.e. Albright et al. (2023); Vial et al. (2023)) are characterized by two populations of cloud chords at the cloud base level. The ~~mean~~ length scale of the first cloud mode $L_1^{CLD}$ (about 150 m) is only slightly smaller than the mean chord length of thermals (170 m in the subcloud layer, 204 m at cloud base), and comparable to the mean chord length of saturated thermals (about 160 m) or cloudy updrafts (about 150 m). It suggests that this cloud population might be rooted in single boundary-layer thermals reaching the condensation level. On the other hand, when there are two distinct cloud populations (i.e. when $L_2^{CLD} \neq L_1^{CLD}$) the length scale of the second one $L_2^{CLD}$ is 739 m on average, which is close to the mean subcloud-layer depth of 725 m (Bony et al., 2022). $L_2^{CLD}$ is thus ~~3 or~~ 4 or 5 times larger (depending on flights) than the mean thermal length ~~$L^{TH}$~~ of cloudy thermals ($L^{THsat}$) or updrafts ($L^{THup}$), which suggests that the second cloud population is fed by several thermals. In the following, we investigate what controls the length scales of these different populations, and how the thermal and cloud chord ~~lengths~~ length distributions relate to each other.

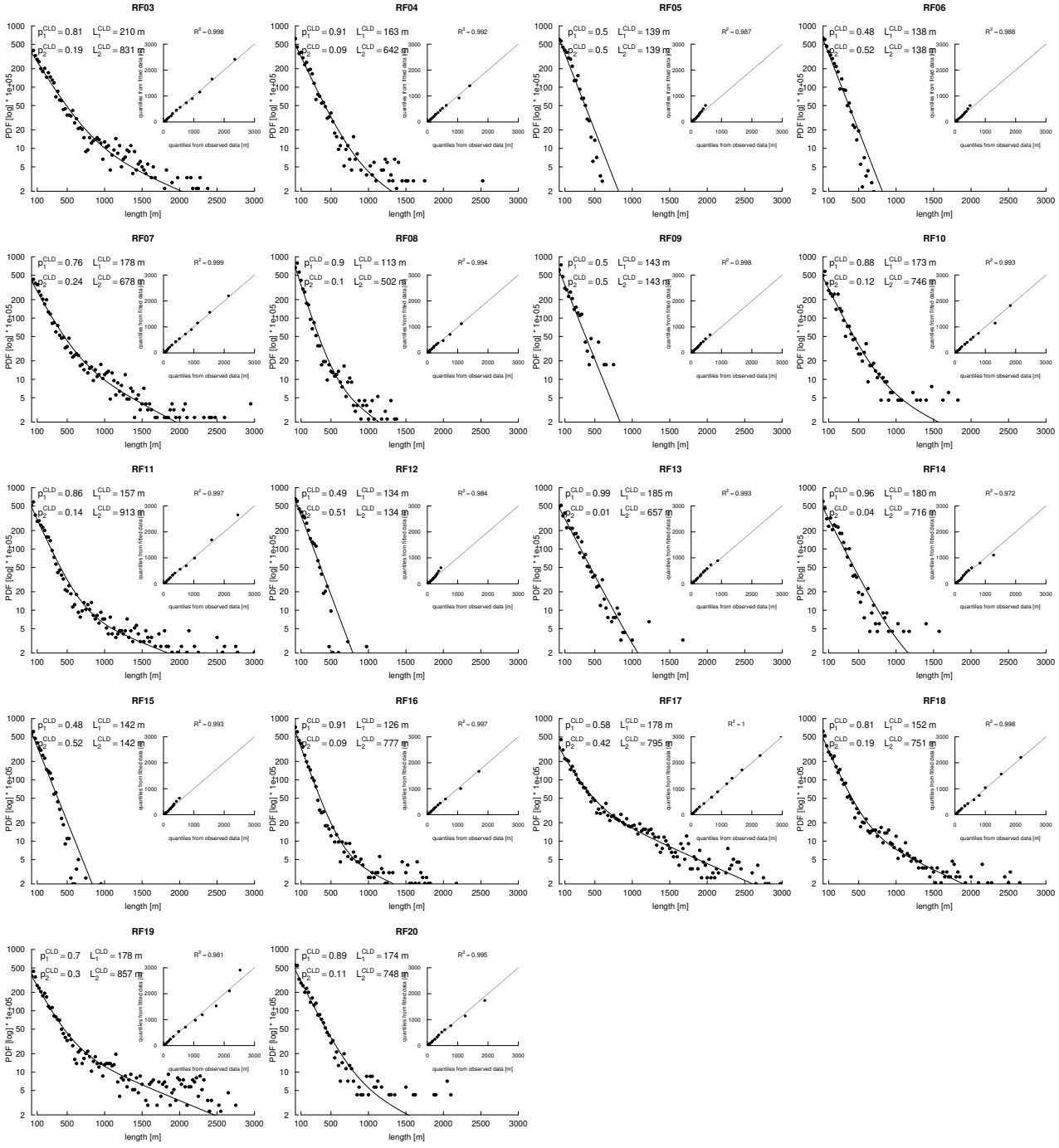


**Figure 5. ~~Cloud~~ Clouds from each EUREC$^4$A flight:** Probability distribution functions of the cloud chord lengths (in meters) derived for each ATR flight from horizontal radar-lidar measurements around the cloud base level. Each panel shows the histogram, its fit by a sum of two exponentials (solid line) and the associated Q-Q plot and $R^2$ (inset) to assess the goodness of fit. The parameters of the fit ($p_1^{cld}$, $L_1^{cld}$, $p_2^{cld}$, $L_2^{cld}$) are also reported.

## 5 Influence of the merging process

EUREC$^4$A observations show that the thermal density decreases with increasing altitude (Table 1), and that the size distribution of thermals changes across the depth of the boundary layer : a single population of thermal chords, whose size is exponentially distributed, is found in the surface layer while two chord populations are found higher up in the subcloud layer and near cloud base (Fig. 1). How to interpret ~~this observed feature~~these observed features?

Based on the theory of fluctuations in an equilibrium convective ensemble, Craig and Cohen (2006) showed that a population of convective objects in statistical equilibrium with its large-scale environment is characterized by an exponential size distribution as long as the objects do not strongly interact with each other. However, it has long been suggested that convective thermals progressively group and merge together with height as they rise through the depth of the subcloud layer (Lenschow and Stephens, 1980; Williams and Hacker, 1993). Simpson et al. (1980) also "postulated merging to be a major way in which convective clouds become larger". Then the question arises as to whether the second population of thermals or clouds (whose average size is several times that of the first population, ~~Table 1~~ Tables 1 and 2) might arise from the interaction of thermals or clouds through a merging process.

If we consider that two objects merge if and only if they touch each other, simple physical reasoning suggests that the efficiency of merging depends on the ratio between the initial average ~~thermal~~ object length $L_0$ and the average ~~thermal~~ object spacing $\lambda_0 = 1/\mathcal{D}_0$, where $\mathcal{D}_0$ is the ~~thermal~~ object density before merging (in the following, the attribute "0" will always refer to quantities *before merging*). ~~However, in reality convective objects such as thermals or clouds might influence each other even without touching, owing to~~

However, fluid mechanical laboratory experiments and simulations have long demonstrated that turbulent thermals and plumes can interact and merge at a distance due to friction and entrainment at their boundaries, ambient horizontal flow or wind shear, buoyancy-induced pressure gradients (Batchelor, 1954; Pera and Gebhart, 1975; Brahimi and Doan-Kim-Son, 1985; Kaye and Lind , and, as we consider further here, the updraft-induced circulation that they create around them ~~(Bretherton, 1987; Poujol, 2025) . As detailed~~ (Bretherton, 1987; Poujol, 2025). As explained in Appendix A and in the Supplementary Information, this is equivalent to considering that the merging takes place between effective objects of size $\beta L_0$ with $\beta \geq 1$, where $\beta$ ~~(~~is referred to as an effective factor~~)~~. For the time being, this parameter can be physically interpreted as ~~being proportional to the lifetime of objects, or to the area~~ the radius of influence an object exerts on other objects through the circulation it induces. Further physical interpretations will be presented in section 6.2.

These physical arguments suggest that the product $\beta\mathcal{D}_0 L_0$ describes a merging efficiency. Then, how does the thermal size distribution depend on ~~$\beta D_0 L_0$~~$\beta\mathcal{D}_0 L_0$? We first address this problem mathematically (section 5.1), and then with a simple numerical statistical model (section 5.2).

### 5.1 Analytical calculations

Let us consider a population of objects (that we will name 'thermals' in the following, but they could be clouds or updrafts in general) randomly placed in space following a uniform distribution, characterized by an averaged length $L_0$, a density $\mathcal{D}_0$, and

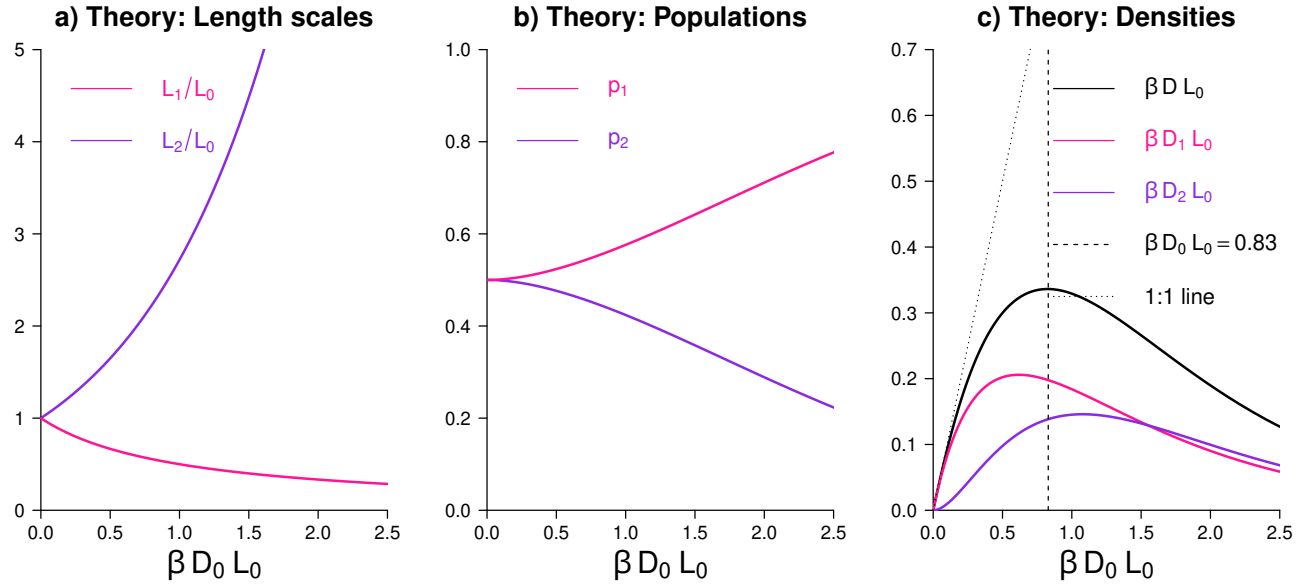


**Figure 6. Theoretical prediction of the impact of merging on the size distribution and densities of chords:** The efficiency of the merging process is quantified by $\beta\mathcal{D}_0 L_0$, where $\mathcal{D}_0$, $L_0$ and $\beta L_0$ are the initial density, length scale and effective length scale of chords before merging. $L_i$ and $p_i$ are the chord length distribution parameters (as defined by equation 1) of the chords that have merged ($L_2$, $p_2$) or not merged yet ($L_1$, $p_1$). Also reported ~~as~~ are the unmerged, merged and total densities ~~$D_1$~~ $\mathcal{D}_1$, ~~$D_2$~~ $\mathcal{D}_2$ and ~~$D = D_1 + D_2$~~ $\mathcal{D} = \mathcal{D}_1 + \mathcal{D}_2$ of chords after merging. The proportion of chords in the first and second populations are given by $\mathcal{D}_1/(\mathcal{D}_1 + \mathcal{D}_2)$ and $\mathcal{D}_2/(\mathcal{D}_1 + \mathcal{D}_2)$, respectively. Note that length scales and densities are undimensioned through a multiplication by $1/L_0$ and $\beta L_0$, respectively.

an exponential size distribution:

$$\mathbb{S}_0(x) = \frac{1}{L_0} e^{-\frac{x}{L_0}} \tag{2}$$

For the reasons explained above and in Appendix A, it is assumed that the merging takes place between objects of effective size $\beta L_0$ with $\beta \geq 1$. It is possible to compute the size distribution of thermals after merging, by distinguishing the two types of thermals that emerge: those that have merged and those that have not merged yet. The analytical treatment (detailed in the Supplementary Material) shows that after letting the thermals merge once or several times, the size distribution of the thermals that have not merged ~~writes:~~ is written:

$$\mathbb{S}_{unmerged}(x) = \frac{1}{L_1} e^{-\frac{x}{L_1}} \text{ with } L_1 = \frac{L_0}{1 + \beta\mathcal{D}_0 L_0} \tag{3}$$

and the size distribution of the thermals that have merged is asymptotically exponential for large thermal sizes ($x \gg L_0$):

$$\mathbb{S}_{merged}(x) = \frac{1}{L_2} e^{-\frac{x}{L_2}} \text{ with } L_2 = L_0 e^{\beta\mathcal{D}_0 L_0} \tag{4}$$

Moreover, analytical expressions are also derived for the density of unmerged thermals, $\mathcal{D}_1$, and the density of merged thermals, $\mathcal{D}_2$, as follows:

$$\mathcal{D}_1 = \mathcal{D}_0 \frac{e^{-\beta \mathcal{D}_0 L_0}}{1+\beta \mathcal{D}_0 L_0} \tag{5}$$

$$\mathcal{D}_2 = \frac{1 - e^{-\beta \mathcal{D}_0 L_0}\left(1 + \frac{\beta \mathcal{D}_0 L_0}{(1+\beta \mathcal{D}_0 L_0)^2}\right)}{\beta L_0 (1 + e^{\beta \mathcal{D}_0 L_0})} \tag{6}$$

After merging, the size distribution of thermals can thus be written as a sum of two exponential functions as written in equation 1, with $L_1$ and $L_2$ defined as above and $p_1 + p_2 = 1$. The calculations indicate that:

$$p_1 = \frac{1}{1 + (1 + \beta \mathcal{D}_0 L_0) e^{-\beta \mathcal{D}_0 L_0}}.$$

$$p_1 = \frac{1}{1 + (1 + \beta \mathcal{D}_0 L_0) e^{-\beta \mathcal{D}_0 L_0}} \tag{7}$$

$$p_2 = \frac{(1 + \beta \mathcal{D}_0 L_0) e^{-\beta \mathcal{D}_0 L_0}}{1 + (1 + \beta \mathcal{D}_0 L_0) e^{-\beta \mathcal{D}_0 L_0}} \tag{8}$$

These calculations, illustrated by Fig. 6, thus show that the merging of thermals that are characterized initially by an exponential size distribution of length scale $L_0$ produces a second population of thermals, and that the size distribution of the thermal population after merging can be represented by the sum of two exponential functions, characterized by two length scales $L_1$ and $L_2$. ~~As illustrated by Fig.6, in~~ In the absence of merging ($\beta \mathcal{D}_0 L_0 = 0$), $L_1 = L_2 = L_0$ ~~and~~ (Fig. 6a) and $p_1 = p_2 = 0.5$ (Fig. 6b): the size distribution can be represented by a single exponential. However, as the merging efficiency $\beta \mathcal{D}_0 L_0$ increases, $L_1$ decreases (because the smaller thermals are statistically less likely to be affected by the merging process) while $L_2$ increases (because the merging produces larger thermals).

The total density of thermals after merging ($\mathcal{D}$, which is always $\leq \mathcal{D}_0$) is the sum of the densities of non-merged and merged thermals~~($\mathcal{D} = \mathcal{D}_1 + \mathcal{D}_2$). Its~~. Using equations 5 and 6, we obtain the following analytical expression:

$$\mathcal{D} = \mathcal{D}_1 + \mathcal{D}_2 \approx \frac{\mathcal{D}_0 e^{-\beta \mathcal{D}_0 L_0}}{1+\beta \mathcal{D}_0 L_0} + \frac{1 - e^{-\beta \mathcal{D}_0 L_0}\left(1 + \frac{\beta \mathcal{D}_0 L_0}{(1+\beta \mathcal{D}_0 L_0)^2}\right)}{\beta L_0 (1 + e^{\beta \mathcal{D}_0 L_0})} \tag{9}$$

Solving the equation $\frac{\partial \mathcal{D}_1}{\partial(\beta \mathcal{D}_0 L_0)} = 0$ shows that there is an optimal $(\beta \mathcal{D}_0 L_0) = \frac{1}{\varphi} \approx 0.618$ (where $\varphi = \frac{1+\sqrt{5}}{2}$ is the golden number) which maximizes the total number of non merged thermals, and that $\mathcal{D}$ reaches a maximum value $\mathcal{D}_{crit} \approx \frac{0.34}{\beta L_0}$ for $\beta \mathcal{D}_0 L_0 = (\beta \mathcal{D}_0 L_0)_{crit} = 0.83$~~(Fig. 6c)~~. There is therefore a critical merging efficiency of thermals beyond which the merging becomes so efficient in producing larger but fewer thermals that the densities of thermals before and after merging become anti-correlated (Fig. 6c). In other words, the $\mathcal{D}$ - $\beta \mathcal{D}_0 L_0$ curve is concave down, with a local maximum at $\beta \mathcal{D}_0 L_0 = 0.83$.

Although the physical meaning of $L_1$ and $L_2$ is clear (these length scales relate to the mean chord lengths of unmerged and merged thermals, respectively), the physical meaning of $p_1$ and $p_2$ is not so clear. When $\beta \mathcal{D}_0 L_0 \to 0$ (i. e., no merging), equations 8 and Fig. 6b show that $L_1 = L_2$ and $p_1 = p_2 = 0.5$. However, when $L_1 = L_2$, any values of $p_1$ and $p_2$ satisfying $p_1 +$

$p_2 = 1$ (including $p_1 = 1$ and $p_2 = 0$) would describe the same (single) exponential size distribution. Therefore, $p_2$ should not be interpreted as the proportion of thermals in the second population (it is just an asymptotic approximation) and the ratio $\frac{\mathcal{D}_2}{\mathcal{D}_1+\mathcal{D}_2}$ is a better measure of the proportion of merged thermals than $p_2$. In addition, the influence of merging on the size distribution is best described by $L_2 - L_1$ or (as will be shown later, Fig. 8b) by the non-dimensional quantity $\frac{L_2-L_1}{2L_0}$, and the absence of merging is best described by $L_2 \to L_1$ or by the density of merged thermals $\mathcal{D}_2 \to 0$.

These calculations thus support our hypothesis that the second exponential of the size distribution results from the merging process. Reciprocally, they also show that it is possible to infer the properties of the thermal population *before* merging from the size distribution of thermals *after* merging (characterized by $L_1$ and $L_2$), ~~using~~: by combining equations 3 and 4 to eliminate $L_0$, we obtain:

$$\beta \mathcal{D}_0 L_0 = W_L\left(e\frac{L_2}{L_1}\right) - 1 \quad \text{where } W_L \text{ is the Lambert W function satisfying} \quad x = W(x)e^{W(x)} \tag{10}$$

and

$$L_0 = L_2 e^{-\beta \mathcal{D}_0 L_0} \text{ or } L_0 \approx \sqrt{L_1 L_2} \tag{11}$$

(the second expression for $L_0$ is obtained after a multiplication of equations 3 and 4, followed by a first order Taylor expansion of the exponential function). Moreover, as shown in the supplementary information, the coverage fraction of thermals can be expressed as:

$$f = \frac{1}{\beta}(1 - e^{-\beta D_0 L_0}). \tag{12}$$

Therefore it is possible to infer $\beta$ in the observations from equations 10 and 12.

### 5.2 Simple statistical simulations

Although analytical calculations support the hypothesis that the merging process is sufficient to explain the presence of a mixture of exponential distributions, they are based on a number of mathematical simplifications that were needed to make the calculations tractable. Therefore we test the validity of the theory and further test the hypothesis that merging can explain the second population of chords in the size distribution of thermals, by developing a simple one dimensional statistical model.

We assume that initially the thermals are uniformly and randomly distributed along a domain of length $L_{domain} = 1000\,\text{km}$ with a mean spacing $\lambda_0 = 1/\mathcal{D}_0$, following a Poisson process, and that they have an exponential size distribution (equation 2) of characteristic size $L_0 = 100\,m$ (this value is chosen to be close to the averaged thermal length measured in the surface layer, Fig. 1a). For the sake of simplicity, we assume $\beta = 1$.

The thermals are placed onto the domain one at a time. Everytime one is placed, it is checked whether the new thermal overlaps with an already existing thermal. If so, then these thermals are merged such that the edges of the new thermal is the leftmost extent of the leftmost old thermal and the rightmost extent of the rightmost old thermal (Fig. A1), as assumed also in the mathematical calculations. After the merging processes takes place, the coverage fraction is counted. If this coverage fraction is less than a pre-specified value $f_{TH}$, then the simulation proceeds by placing a new thermal, checking for overlap,

merging if there is overlap, then computing the coverage fraction again. This continues until the coverage fraction in the simulation equals ~~a pre-specified value~~ $f_{TH}$. Once they are equal, the simulation is ended. The simulation is then repeated 10 times to generate more statistics. The thermal positions and lengths are recorded both before and after the merging process takes place.

Fig. 7a shows the chord length distributions obtained through this process for a range of $f_{TH}$ values, which (from equation 12) amounts to a range of $\beta \mathcal{D}_0 L_0$ values and thus of merging efficiencies. ~~Although in~~ In the case of weak merging efficiency, the final distribution is close to the initial exponential distribution. However, for stronger merging efficiencies we note the formation of larger chords and an increasing deviation from the initial distribution, with the formation of long tail. Each final distribution turns out to be well fitted by a sum of two exponentials. As merging is the only process represented in this model, it shows that if the initial size distribution of thermals is exponential, merging is a sufficient process to explain the formation of a second population of larger thermals and produce a final chord length distribution that is well fitted by a double exponential.

This is further confirmed by Fig. 7b that shows the decomposition of the size distribution into merged and unmerged thermals for a given merging efficiency. Although the size distribution of the thermals that have not merged yet is exponential and associated with a shorter lengthscale than the initial distribution ($L_1 < L_0$), the size distribution of the thermals that have merged tends, for large chord lengths, to an exponential distribution. This is in line with the theory that predicts that the distribution of merged thermals is only asymptotically exponential (that is, for lengths much larger than $L_0$).

We then use the simple model to assess the ability of the analytical calculations to predict $L_1$, $L_2$ and the thermal densities. Although not perfect, we note a fairly good agreement between simulations and theoretical predictions, both for the ~~lengthscales~~ length scales (Fig. 7c) and for the evolution of the densities of merged and unmerged thermals with the merging efficiency (Fig. 7d). These results give us confidence in the validity of the analytical treatment, and encourage us to use this theory to interpret the observations.

## 6 Interplay between thermals and clouds

### 6.1 Thermal merging inferred from observations

Given that trade wind clouds are rooted in subcloud layer thermals (LeMone and Pennell, 1976), we now investigate how the merging of boundary layer thermals imprints the size distribution of clouds near their base. For this purpose, we first assess the extent to which the physical framework presented in section 5 can help interpret EUREC$^4$A observations (summarized in Tables 1 and 2). From equations 10 and 11 and the length scales $L_1$ and $L_2$ inferred from the observed chord length distributions, we infer $L_0$ and $\mathcal{D}_0$. From equation 12 and the fractional coverage of thermals or clouds measured for each flight, we infer $\beta$. Then, from the values of ($\mathcal{D}_0$, $L_0$, $\beta$) associated with each flight, we compute the density of thermals expected from the theory (equation 9) and compare it with the density that was actually measured during the campaign.

For most of the flights there is a good agreement, both in the subcloud layer and near cloud base (Fig. 8a). Since the measured thermal density was not used to diagnose ($\mathcal{D}_0$, $L_0$, $\beta$), this can be considered as an independent consistency test of the theory

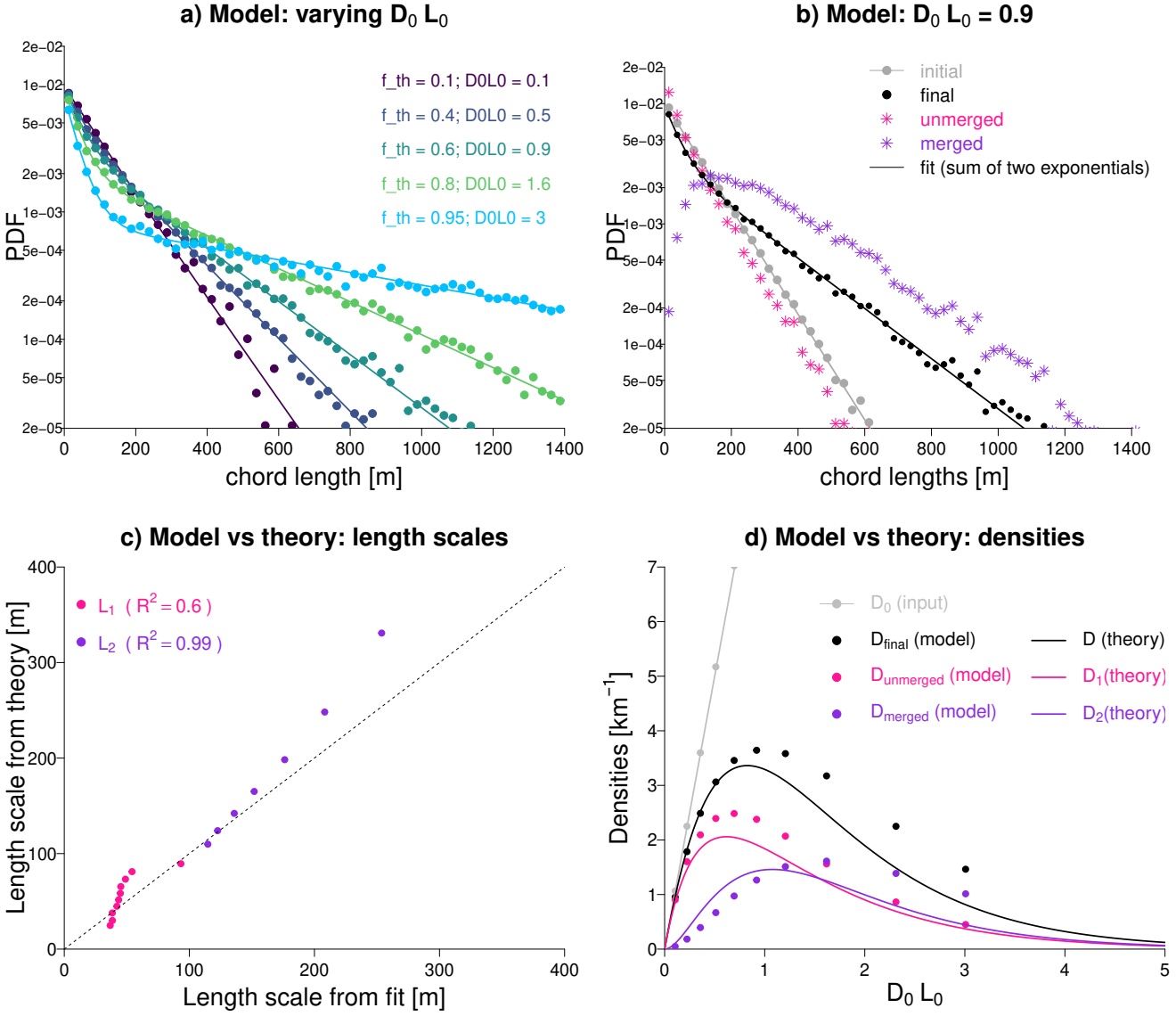


**Figure 7. Simple statistical model of chord merging:** (a) Chord length distributions obtained for $L_0$ = 100 m, $\beta = 1$ and different values of $f_{TH}$ (or, equivalently, for a range of $\beta\mathcal{D}_0 L_0$ values), fitted by a sum of two exponential functions (solid lines). (b) For a particular value of the merging efficiency ($\beta\mathcal{D}_0 L_0 = 0.9$ or $f_{TH} = 0.6$), comparison of the chord length distributions of thermals before merging (in grey) and after merging, considering all thermals (in black) or just those that have merged (in ~~blue~~purple) or that remain unmerged (in ~~red~~pink). The initial and unmerged thermals are well fitted by a single exponential distribution while the distribution of merged thermals tends asymptotically (for chord lengths $\gg L_0$) towards an exponential distribution. (c) Comparison of the distribution length scales $L_1$ (in ~~red~~pink) and $L_2$ (in ~~blue~~purple) predicted by theory or actually obtained from the fit of chord length distributions for a range of $\beta\mathcal{D}_0 L_0$ values. (d) Comparison between the simple statistical model and the theory of the chord density $\mathcal{D}$ after merging, and its decomposition into $\mathcal{D}_1$ (unmerged, in ~~red~~pink) and $\mathcal{D}_2$ (merged, in ~~blue~~purple). The chord density before merging ($\mathcal{D}_0$, in grey) is also reported.

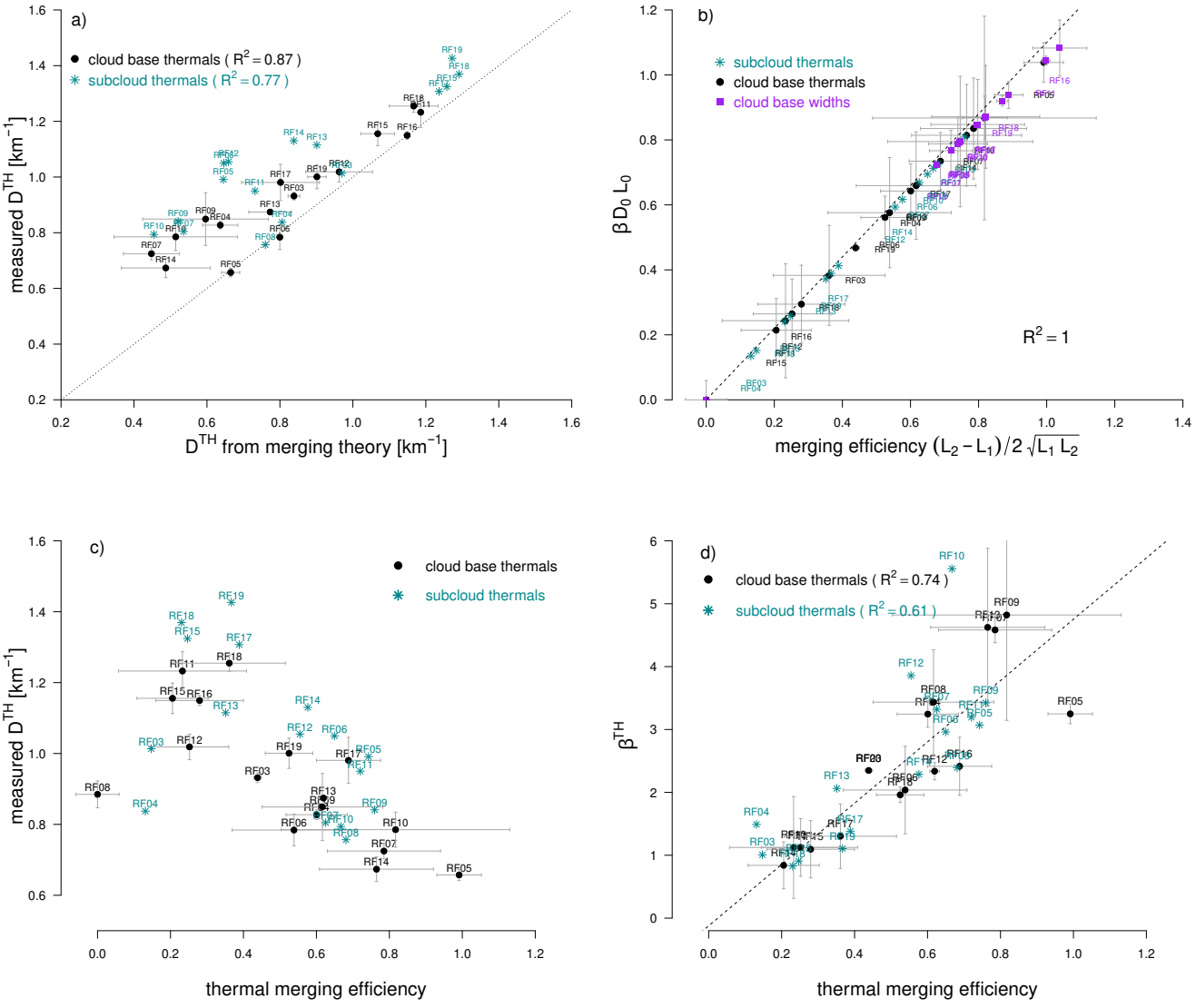


**Figure 8. Consistency between theory and observations:** (a) Comparison of the density of thermals after merging derived from turbulence measurements or predicted from theory using equation 9. Each point represents one ATR research flight (Table 1). Horizontal and vertical bars represent errors on the mean calculated from the measurements associated with the different rectangles flown near cloud base. Turquoise and black markers correspond to thermals sampled in the subcloud layer and near the cloud base, respectively. (b) Relationship (shown for thermals and clouds) showing the equivalence between the theoretically defined merging efficiency $\beta \mathcal{D}_0 L_0$ and the quantity ($L_2$-$L_1$)/($2L_0$) derived from chord length distributions. (c) Relationship between the thermal merging efficiency, defined as ($L_2$-$L_1$)/($2L_0$), and the measured thermal density (after merging). The relationship is shown for thermals sampled either in the subcloud layer or near cloud base. (d) Relationship between the effective length parameter of thermals $\beta^{TH}$ and the thermal merging efficiency. A value larger than one means that thermals influence each other even without touching owing to the return circulation they induce around them. In a) and b) the dashed line is a 1:1 line, and in d) it is the linear regression line for the cloud base thermals. Error bars correspond to standard errors around the mean estimated from the two or three rectangles flown at cloud base during each flight.

with the observations. Moreover, since the theoretical prediction of the density is based only on the effect of the merging process, it suggests that the variability of the thermal density over the course of the campaign primarily reflects the effect of the variability of the merging process on the thermals field. ~~Neverthess~~Nevertheless, there are a few discrepancies at the lowest density values, where observations report a higher thermal density than predicted by the theory. In these cases, the thermal density seems to depend not only on the merging process, but also on other factors. These factors probably include the influence of the low-level convergence associated with the circulations created by cloud updrafts or shallow mesoscale circulations such as those revealed by George et al. (2023), which can increase the thermal density below the clouds (Rousseau-Rizzi et al., 2017) but are not included in the merging theory, nor in the simple statistical simulations.

In the analytical calculations, the strength of the merging process is quantified by $\beta \mathcal{D}_0 L_0$. As the merging of objects of initial length scale $L_0$ results in a size distribution of objects characterized by length scales $L_1 \leq L_0$ and $L_2 \geq L_0$, we expect $L_2$ - $L_1$ to vary together with $\beta \mathcal{D}_0 L_0$. This is indeed what we find (Fig. 8b), with $(L_2 - L_1)$ varying linearly with $\beta \mathcal{D}_0 L_0$ and $(L_2 - L_1)/(2\,L_0) \approx \beta \mathcal{D}_0 L_0$ for both thermals and clouds. It suggests that the metric $(L_2 - L_1)/(2L_0) \approx (L_2 - L_1)/(2\sqrt{L_1 L_2})$, which is derived directly from the fit of the observed chord length distributions, can be used as a simple proxy for the merging efficiency of thermals or clouds.

The variation of the thermal density with the merging efficiency of thermals is shown on Fig. 8c. As predicted by the theory and the simple model (section 5), the correlation between these two variables is positive for weak merging efficiencies and negative for stronger merging efficiencies. This anti-correlation is explained by the fact that the merging process produces larger but fewer thermals, which reduces the thermal density. However, we note that in observations the anti-correlation starts at a lower value of the merging efficiency than in Fig. 6c or 7d. This is because in Nature the effective area of influence of a thermal is larger than the thermal size itself ($\beta > 1$) owing to the circulation induced by the thermal around it (Bretherton, 1987; Poujol, 2025), and there is a positive correlation between the merging efficiency and $\beta$ (Fig. 8d). This makes the merging even more efficient in reducing the thermal density than in the absence of such a circulation.

### 6.2 Physical interpretation of $\beta$

Figure 8d suggests that the flight-to-flight variability in merging efficiency is primarily governed by variations in $\beta$. Therefore it is important to clarify the physical interpretation of this parameter.

As explained in section 5, $\beta$ was introduced in the merging framework to capture the ability of convective objects to interact and attract each other without direct contact, thereby facilitating merging. For thermals or clouds, which transport air upward in an updraft, such interactions can arise from the circulations induced around them as a consequence of mass conservation (Bretherton (1987); Poujol (2025), Appendix A). In this context, $\beta$ can be interpreted as the radius of influence (or basin of attraction) that an object exerts on its surroundings through the circulation it generates. In other words, $\beta$ corresponds to the region where a given thermal can capture its neighbours through the circulation it creates. Since objects probably move to achieve the merging process, the amount of movement depends on $\beta$. However, $\beta$ may also encapsulate other mechanisms, such as the effects of imposed mass convergence in the subcloud layer (for instance, induced by an overlying cloud or associated with an external circulation), which increases thermal density (Rousseau-Rizzi et al., 2017) and thereby enhances merging.

Several other interpretations can be inferred from the definition of $\beta$ (Appendix A): $\beta = 1 + \frac{H}{h}\frac{T_{life}}{T_{transit}}$, where $T_{life}$ is the lifetime of the updraft and $T_{transit}$ the time necessary for an air parcel to travel from the bottom to the top of the updraft. The ratio $T_{life}/T_{transit}$ can be viewed as the number of successive warm bubbles ($N_{bubbles}$) that rise over the course of the life of an updraft. Therefore, a persistent, long-lived convective system will be associated with a large $\beta$.

Finally, for clouds $\beta$ can also be expressed in terms of the ratio between the area of the anvil of the cloud and its core size. Indeed, if the cloud core size is $L_{core} = L_A$, and $u_A$ is the horizontal velocity of the outflow layer, the cloud anvil size is given by $L_{anvil} = 2u_A T_{life}$. Therefore we get: $\frac{L_{anvil}}{L_{core}} = \frac{2u_A T_{life}}{L_A} = \frac{H}{h'}\frac{T_{life}}{T_{transit}}$ where $h'$ is the depth of the outflow layer at the cloud top and $H$ is the depth of the updraft. $\beta$ is thus directly related to the (aspect) ratio between the size of the anvil and the size of the cloud core.

To summarize, $\beta$ quantifies the effect (in space and time) of convective-scale circulations on the merging of thermals or clouds. It increases with the radius of influence that a convective object exerts on its surroundings through the circulation it generates, with the lifetime of the convective object and, in the case of clouds, with the aspect ratio of the cloud field:

$$\beta = 1 + \frac{H}{h}\frac{T_{life}}{T_{transit}} \tag{13}$$

$$= 1 + \frac{H}{h} N_{bubbles} \tag{14}$$

$$= 1 + \frac{h'}{h}\frac{L_{anvil}}{L_{core}} \tag{15}$$

Because the life time of an updraft is usually at least as long as the transit time, $\beta$ is always larger than 1, and is typically of a few units (it actually ranges between 1 and 5 in the case of thermals, Fig. 8d). However, as shown later (Fig. 12d), it can reach much larger values (5 to 30) for long-lived updrafts that typically produce extensive anvil clouds, as observed in Flowers.

### 6.3 From thermal merging to cloud populations

Having checked the consistency of the observations with the theory, we can now further interpret the observations in the light of the merging theory. ~~We can only measure the result of the merging process. However, using~~ Using equations 10 and 11 we can estimate the length scale of objects that, after merging, would lead to size distribution length scales ($L_1$ and $L_2$) similar to those observed, and thus obtain clues as to the origin of the merged ~~thermals~~objects. This is done using the thermal chord length distributions measured near the ocean surface, in the subcloud layer and near cloud base and using the cloud base width distributions.

Figure 9a shows that in the surface layer, $L_0^{TH}$ estimates (97 m $\pm$ 24 m) are very close to the mean size $L^{TH}$ of thermals (97 m $\pm$ 22 m) and to $L_1^{TH}$ in that layer (Table 1). It suggests that at that level, thermals experience very little merging and remain largely independent of each other. Within the subcloud layer and near cloud base, on the other hand, $L_0^{TH}$ estimates (159 m $\pm$ 27 m and 172 $\pm$ 26 m, respectively) are close but smaller than the mean thermal sizes found at the same level ($L^{TH}$ = 170 m $\pm$ 45 m in the subcloud layer and 204 m $\pm$ 42 m near cloud base). The thermal size distributions measured within the

subcloud layer and near cloud base are thus consistent with those expected from the merging of thermals through the depth of the subcloud layer.

Figure 9b shows the $L_0^{CLD}$ values inferred for each flight from $L_1^{CLD}$ and $L_2^{CLD}$ (Fig. 5). In this case, $L_0^{CLD}$ is bimodal: in the presence of a single cloud population, $L_0^{CLD} \approx L_1^{TH}$ (measured near cloud base or in the subcloud layer) $\approx L_1^{THsat}$, while in the presence of two cloud populations, $L_0^{CLD} \approx L_2^{TH}$ (measured near cloud base or in the subcloud layer) ~~. It suggests that as anticipated in section 4 (large cloud bases are fed by several thermals ), unmerged thermals are the roots of~~ $\approx L_2^{THsat}$ (the close relationship between the thermal length scales and $L_0^{CLD}$ is further illustrated in Fig. S2). Moreover, the density of clouds prior to merging $\mathcal{D}_0^{CLD}$ correlates well with the density of cloudy thermals $\mathcal{D}^{THsat}$ (Figs. 9c) or updrafts $\mathcal{D}^{THup}$ and is of a similar order of magnitude. In fact, $\mathcal{D}_0^{CLD}$ is slightly higher than $\mathcal{D}^{THsat}$, suggesting that the merging may involve not only cloudy thermals but also, to a lesser extent, clouds that are not – or no longer – rooted in active thermals.

It thus appears that unmerged thermals that overshoot the LCL form the first population of (very shallow) clouds, and ~~that merged thermals are the roots of clouds~~ merged thermals that overshoot the LCL generate cloud shoots which, after merging with each other and/or with unmerged saturated thermals, form the second population of clouds, that are on average wider and deeper. The merging of thermals and cloud shoots thus exerts a strong control on the type of clouds present.

A schematic of the impact of the merging process on thermals and clouds is represented in the lower half of Figure 10: turbulence near the surface produces a large density of thermals. As they rise across the depth of the subcloud layer, some of them merge and become wider. This results in two thermal populations coexisting in the subcloud layer and near cloud base: those that have merged (of length scale $L_2^{TH}$), and those that have not merged yet (of length scale $L_1^{TH}$). As a result of merging, the thermal density decreases with height. The thermals that overshoot the lifting condensation level (about one out of five on average during EUREC$^4$A) saturate at their top and form 'cloud shoots' whose base has initially the same size as the saturated thermals that produced them ($L_0^{CLD} \approx L_1^{TH} \approx L_1^{THsat}$ or $L_0^{CLD} \approx L_2^{TH} \approx L_2^{THsat}$, Fig. 9b). As will be shown later (Fig. 12c), a higher density of thermals ($\mathcal{D}^{TH}$) is associated with a higher density of saturated thermals $\mathcal{D}_{sat}^{TH}$ (Fig. S5, consistent with the fact that when the density of thermals is high, the boundary layer is moister and the LCL is lower) and thus a higher density of 'cloud shoots' ($\mathcal{D}_0^{CLD}$, Fig. 9c). When cloud shoots form close to each other (which occurs more easily when thermal merging is weak and thus the thermal density around cloud base is high), they can merge. It forms larger bases and leads to the formation of wider and deeper clouds.

## 7 Implications of the merging process on clouds and circulations at larger scales

Observations thus reveal a strong relationship between thermal merging and clouds. In this section, we explore its implications for the mesoscale organisation of convection and trade wind cloudiness. During the four weeks of the EUREC$^4$A campaign, shallow convection and clouds exhibited a variety of mesoscale organisations and patterns. Based on modeling studies (Bretherton and Blossey, 2017; Narenpitak et al., 2021; Janssens et al., 2023), we expect the transitions between different patterns to be related to the development of shallow mesoscale circulations, which themselves depend on the convective mass flux. We also expect the different patterns of cloudiness to embed different cloud populations (Stevens et al., 2020), and the convective

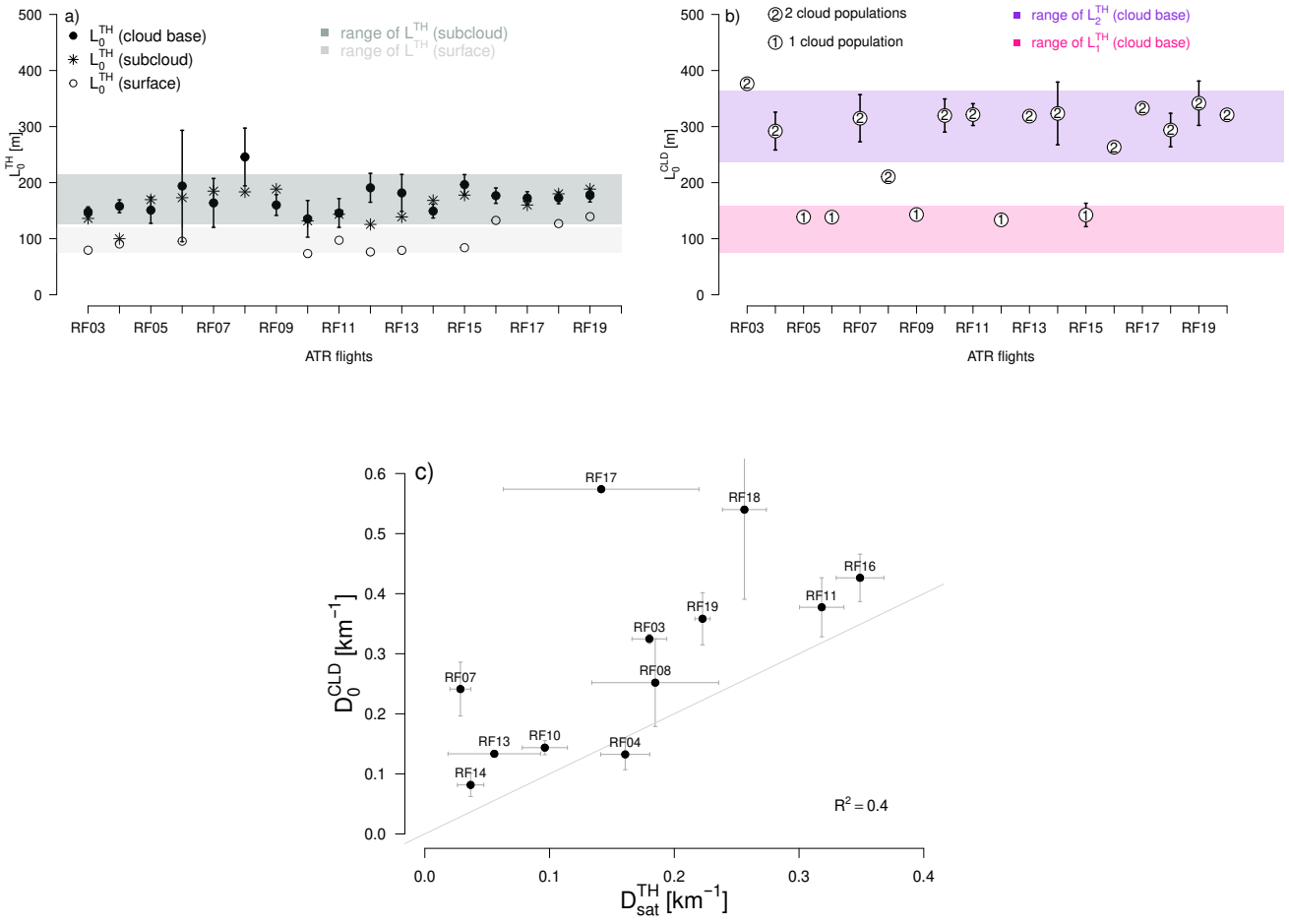


**Figure 9. Origin of merged thermals and relationship between thermals and clouds:** (a) Length scale of thermals before merging ($L_0^{TH}$) ~~inferred from theory (section 5.1) and ($L_1^{TH}$, $L_2^{TH}$)~~ calculated for each ATR flight near the ocean surface, within the subcloud layer ~~or~~ and near cloud base (vertical bars represent the standard error on the mean calculated for each flight on the basis of the repeated flight patterns flown around the cloud base level); $L_0^{TH}$ values are compared to the range (mean $\pm$ standard deviation) of mean thermal lengths ($L^{TH} = p_1^{TH} L_1^{TH} + p_2^{TH} L_2^{TH}$) measured in the surface layer (~~in green~~light grey) and within the subcloud layer (~~in brown~~darker grey). (b) Length scale of clouds before merging ($L_0^{CLD}$) compared to the range of $L_1^{TH}$ (pink) and $L_2^{TH}$ (~~the shading shows the range near~~ purple) at cloud base~~and~~. For each flight, the ~~vertical bars~~ number reported on the ~~right show~~ marker indicates whether this flight was associated with one or two cloud populations. $L_0^{CLD} \approx L_1^{TH}$ in the ~~range within~~ presence of a single cloud population, while $L_0^{CLD} \approx L_2^{TH}$ in the ~~subcloud layer~~presence of two cloud populations. (c) Relationship between the density of saturated thermals $\mathcal{D}^{THsat}$ and the cloud density before merging $\mathcal{D}_0^{CLD}$ (the grey line shows the 1:1 line). Saturated thermals may be considered as incipient cloud bases or 'cloud shoots'.

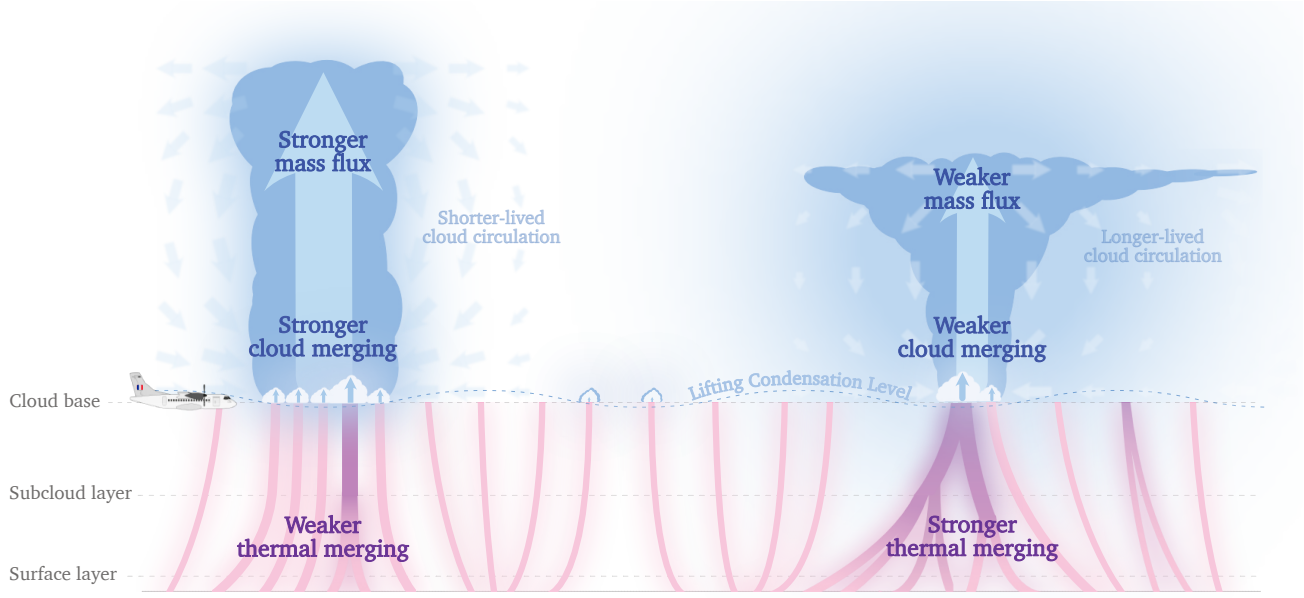


**Figure 10. The thermal and cloud merging process (profile view)**. Each thermal (pink or purple) or cloud (blue) is represented by an updraft. Two objects (thermal or cloud) can merge if they touch each other. However, each convective object exerts an attraction on other objects in its vicinity (shaded area) due to the circulation it creates around itself (Appendix A). Therefore, two objects can merge even without touching if their areas of influence overlap. This makes the merging process more efficient (in the analytic framework, this effect is encapsulated by the effective factor $\beta \geq 1$). Turbulence in the surface layer generates a high density of small thermals that are initially unmerged (pink). These thermals have an exponential size distribution and a mean size $L_0^{TH}$. As they rise across the depth of the subcloud layer, some of them merge (purple) and become wider. This results in two populations of thermals coexisting in the subcloud layer and near cloud base. The size distribution of these populations can be represented by the sum of two exponentials, each with a characteristic size $L_1^{TH} \leq L_0^{TH}$ and $L_2^{TH} \geq L_0^{TH}$. When the depth of the thermals exceeds the lifting condensation level (whose height varies spatially and tends to be lower in moister areas), incipient cloud bases form (~~light blue~~white clouds). ~~Those arising from unmerged thermals~~ The base of these 'cloud shoots' has initially ~~have a mean~~ the same size as the saturated thermals that produced them ($L_0^{CLD}$ ~~=~~ $\approx L_1^{TH}$ ~~, while those arising from merged thermals initially have a mean size~~ $\approx L_0^{CLD}$ ~~$= L_2^{TH}$~~ $L_1^{THsat}$ or $L_2^{TH} \approx L_2^{TH} \approx L_2^{THsat}$). When cloud ~~bases~~ shoots form close to each other (which occurs more easily when thermal merging is weak and therefore the thermal density is high around cloud base), they can merge. It forms larger bases (dark blue) and leads to the formation of deeper clouds. The merging process thus leads to a spectrum of clouds whose chord lengths distribution around cloud base can be represented by a sum of two exponentials with characteristic sizes $L_1^{CLD}$ and $L_2^{CLD}$. In EUREC$^4$A, $L_1^{CLD}$ is close to the average size of thermals that overshoot the LCL (150-160 m), while $L_2^{CLD}$ is close to the ~~average~~ depth of the subcloud layer on average, but varies strongly with merging conditions.

mass flux to influence the cloud fraction near cloud-base (Vogel et al., 2022). Thanks to the repeated flight plan of the ATR during the campaign, we can compare the different flights to each other and shed light on the role of thermal merging in these co-variations.

### 7.1 Convective mass flux and shallow mesoscale circulations

Each ATR flight was typically associated with two to three hours of in-situ and remote sensing measurements around the cloud base level. During this time, HALO was dropping $3 \times 12$ dropsondes along three consecutive, 200 km diameter circles (Stevens et al., 2021). From these dropsondes, a horizontal wind divergence and then an area-averaged mesoscale vertical velocity could be estimated (Bony and Stevens, 2019; George et al., 2021, 2023). From the vertical velocity measured around cloud base ($W_b$) and an analysis of the subcloud layer mass budget (Albright et al., 2022), an area-averaged mass flux $M_b$ could also be estimated (Vogel et al., 2020, 2022). In addition, by using high frequency (25 Hz) in-situ measurements of vertical velocity and humidity from the ATR (Brilouet et al., 2021), we could estimate a linear cloud-base mass flux along the ATR trajectory as $M_b^{ATR} = \Sigma_i \rho_i a_i w_i$, with $a_i = H(rh_i - 0.98)/N$, where $H$ is the Heaviside function, $rh_i$ and $w_i$ are the relative humidity and vertical velocity (assuming zero mean vertical velocity over each 30 km segment) measured in each point $i$ of the trajectory, N is the total number of measurements made at the cloud base level for each flight, and $\rho_i$ is the air density assumed to be 1 kg.m$^{-3}$ for simplicity (see Lamer et al. (2015) for a justification of these approximations).

Despite differences during flights where the spatial scale of the cloud organization was larger than the region sampled by the ATR (e.g. RF14), the two independent $M_b$ estimates exhibit the same large flight-to-flight variability, and both correlate positively with the density of thermals near the cloud base level (Figure 11a). From Vogel et al. (2022) we know that $M_b$ co-varies with the mesoscale vertical motion around cloud base ($W_b$), and indeed ascending branches of mesoscale circulations ($W_b > 0$) tend to be associated with stronger $M_b$ than subsiding branches (Fig. 11b). We also note that shallow mesoscale circulations tend to be associated with a heterogeneous distribution of thermals, as thermals are more concentrated in regions of mesoscale ascent and low-level convergence and more sparse in regions of low-level divergence. However, the relationship between thermal density and $W_b$ exhibits some outliers. They may be due to the presence of cold pools (e.g. during RF17 and RF18 that were associated with a strong precipitation), which affect the low-level divergence and therefore the measurement of mesoscale vertical motions (Touzé-Peiffer et al., 2022), and likely modulate the distribution of thermals. The relationship between the thermal density inferred from ATR turbulence measurements and the $M_b$ or $W_b$ estimates inferred from HALO dropsondes might also be affected by the different area and time samplings of the two aircraft (e. g. during RF17).

What controls the magnitude of $M_b$? Since the cloud-base mass flux is known to be more strongly modulated by the cloud size than by the in-cloud vertical velocity (Dawe and Austin, 2012; Vogel et al., 2022), we expect higher values of $M_b$ to be related to the presence of wider clouds. Indeed, when two cloud populations are present, $M_b$ increases with the length scale of the second cloud population (Fig. 11c), which increases with the merging efficiency of clouds (Fig. 11d, section 5). The flight-to-flight variations in $M_b$ can also be interpreted as a result of variations in the thermal population. Noting that $M_b$ can be well approximated by the product of the mean density, length and vertical velocity of cloudy thermals $M_b \approx w_{sat}^{TH} . \mathcal{D}_{sat}^{TH} . L_{sat}^{TH}$ (Fig. S6 of the Supplementary Information), it appears that $M_b$ variations are primarily governed by $\mathcal{D}_{sat}^{TH}$ variations (and to a

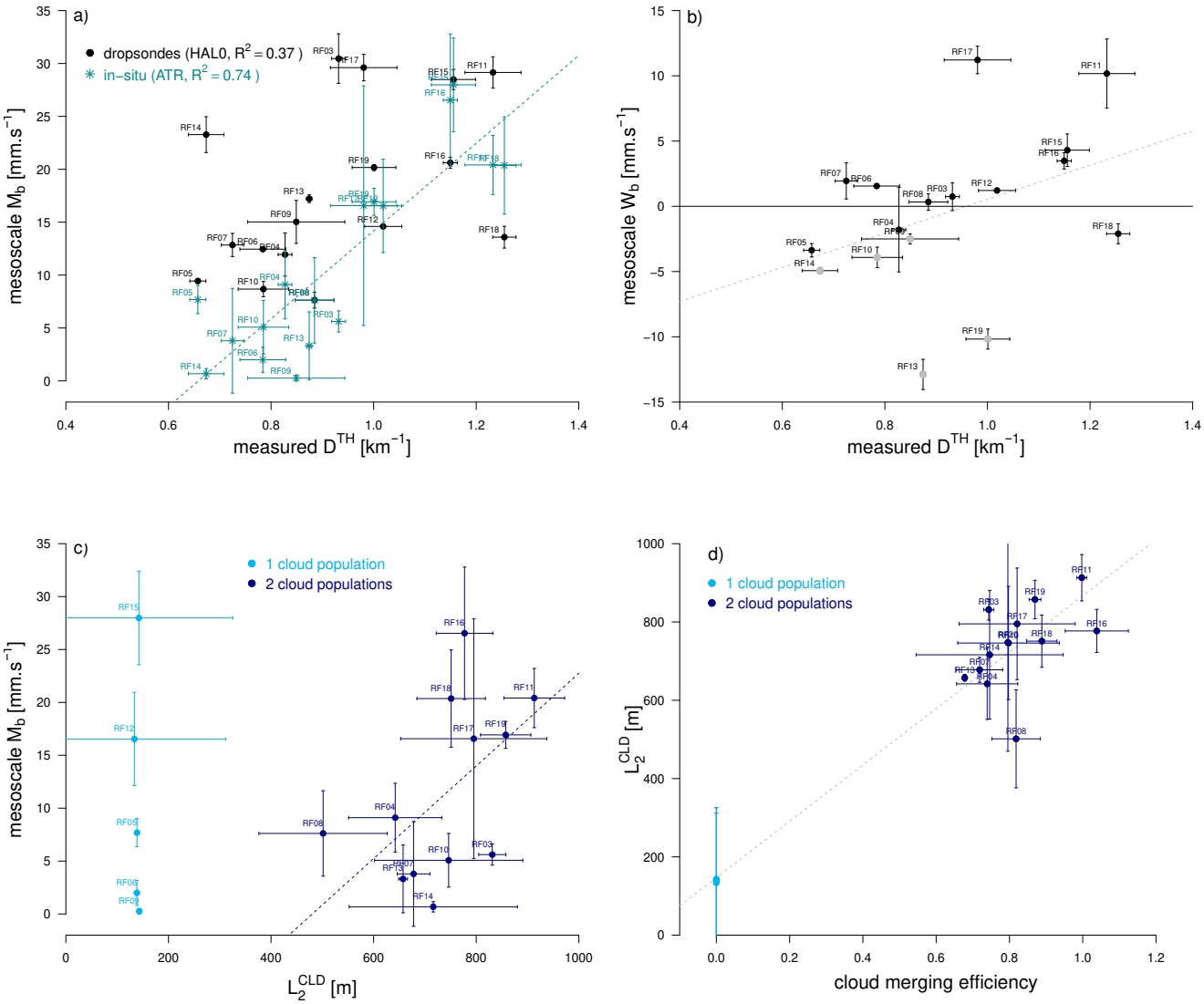


**Figure 11. Convective mass flux and shallow mesoscale circulations:** Relationship between the thermal density $\mathcal{D}^{th}$ measured around cloud base and (a) the domain-averaged mass flux $M_b$ (derived either from dropsondes and the mass budget of the subcloud layer or from in-situ turbulence measurements) and (b) the mesoscale vertical velocity $W_b$ inferred from dropsondes near the cloud-base level (grey markers correspond to the flights whose mixed layer depth suggests that they were influenced by cold pools). (c) Relationship between the cloud lengthscale $L_2^{CLD}$ and the convective mass flux $M_b$ (note that $L_2^{CLD} = L_1^{CLD}$ when only one cloud population is present) and (d) between the cloud lengthscale $L_2^{CLD}$ and the cloud merging efficiency (defined as $\left(\frac{L_2 - L_1}{2\,L_0}\right)^{CLD}$ or as $(\beta \mathcal{D}_0 L_0)^{CLD}$). In (c) and (d), all quantities are derived from ATR measurements. In each panel, each point represents one ATR flight. Horizontal and vertical bars represent standard errors on the mean, inferred from the variability of measurements during each flight.

lesser extent by $w_{sat}^{TH}$ variations), which are roughly proportional to variations of total density of thermals $\mathcal{D}^{TH}$ (Fig. S5). In other words, ~~the clustering of clouds makes wider clouds and increasesthe convective~~ a weaker thermal merging is associated with a higher density of thermals ($\mathcal{D}^{TH}$) and saturated thermals ($\mathcal{D}_{sat}^{TH}$); this leads to a higher density of cloud shoots ($\mathcal{D}_0^{CLD}$, Fig. 9c) and thus promotes cloud merging and the formation of wider cloud bases ($L_2^{CLD}$ increases), which eventually leads to a stronger mass flux.

However, we note that sometimes a strong mass flux can occur in the absence of cloud ~~clustering~~ merging (Fig. 11c): in RF15 we observe only one cloud population, and the strong mass flux comes from the many small clouds that form on top of a very high density of thermals. In fact, the comparison of RF15 with the following flight (RF16, which occurred a few hours later on the same day) shows that the many small clouds of RF15 later began to merge and form a second population of clouds with wider cloud bases.

What role does the thermal-cloud coupling play in mesoscale circulations? The theoretical study of ~~Janssens et al. (2023)~~ Janssens et al. (2023, 2024) showed that cumulus mass fluxes favor the development of mesoscale ascents, and the modeling study of Rousseau-Rizzi et al. (2017) showed that the low-level mass convergence associated with mesoscale ascents increases the density of thermals in the subcloud layer. EUREC$^4$A observations support these results, but also suggest that a high density of thermals will eventually favor thermal merging, resulting in fewer and wider but more widely spaced thermals. This will reduce cloud merging, and thus $M_b$, potentially to the point where $W_b$ will become less ascending or even descending. In this way, thermal merging is likely to temper, or act as a negative feedback, on the growth of shallow mesoscale circulations.

### 7.2 Mesoscale patterns of cloudiness

A large variability of cloud mesoscale patterns was observed during the EUREC$^4$A campaign (Schulz, 2022), with the occurrence of each of the four known prominent patterns of tradewind cloudiness (Stevens et al., 2020; Bony et al., 2020). However, most flights were associated with a mixture of cloud mesoscale organizations, and sometimes the ATR was sampling an area smaller than the scale of the cloud pattern itself (e.g. during RF09 the ATR spent most of its flight time in between the cloud systems that constitute the Flower pattern, Bony et al. (2022)). In Fig 12, we highlight the five flights associated with only one cloud population (in green), and six flights (out of 14) associated with two cloud populations and either high or low thermal densities (in orange and red, respectively). An additional flight is highlighted (RF08), which is associated with only one population of (large) thermals (Table 1). The cloud patterns present on these different days are illustrated with satellite images (bottom of Fig. 12~~c~~). How do they differ in terms of thermal and cloud merging?

Fig. 12a-b show that the measured thermal density is anti-correlated with the strength of thermal merging, and that cloud merging is anti-correlated with thermal merging. These features can be explained as following: when there is little thermal merging, the thermals are small but numerous (~~$\mathcal{D}^{th}$~~ $\mathcal{D}^{TH}$ is large), and therefore the clouds rooted in these thermals form close to each other. Since $\beta^{CLD} > \beta^{TH}$, the clouds merge more easily than thermals, forming wider cloud bases (Fig. 11d). In contrast, a strong merging of thermals leads to wider but sparser thermals (~~$\mathcal{D}^{th}$~~ $\mathcal{D}^{TH}$ is small); the clouds forming on top of these thermals are thus initially wider (because $L_0^{CLD} = L_2^{TH}$ and $L_2^{TH}$ increases with thermal merging) but are more widely spaced and therefore they merge less easily.

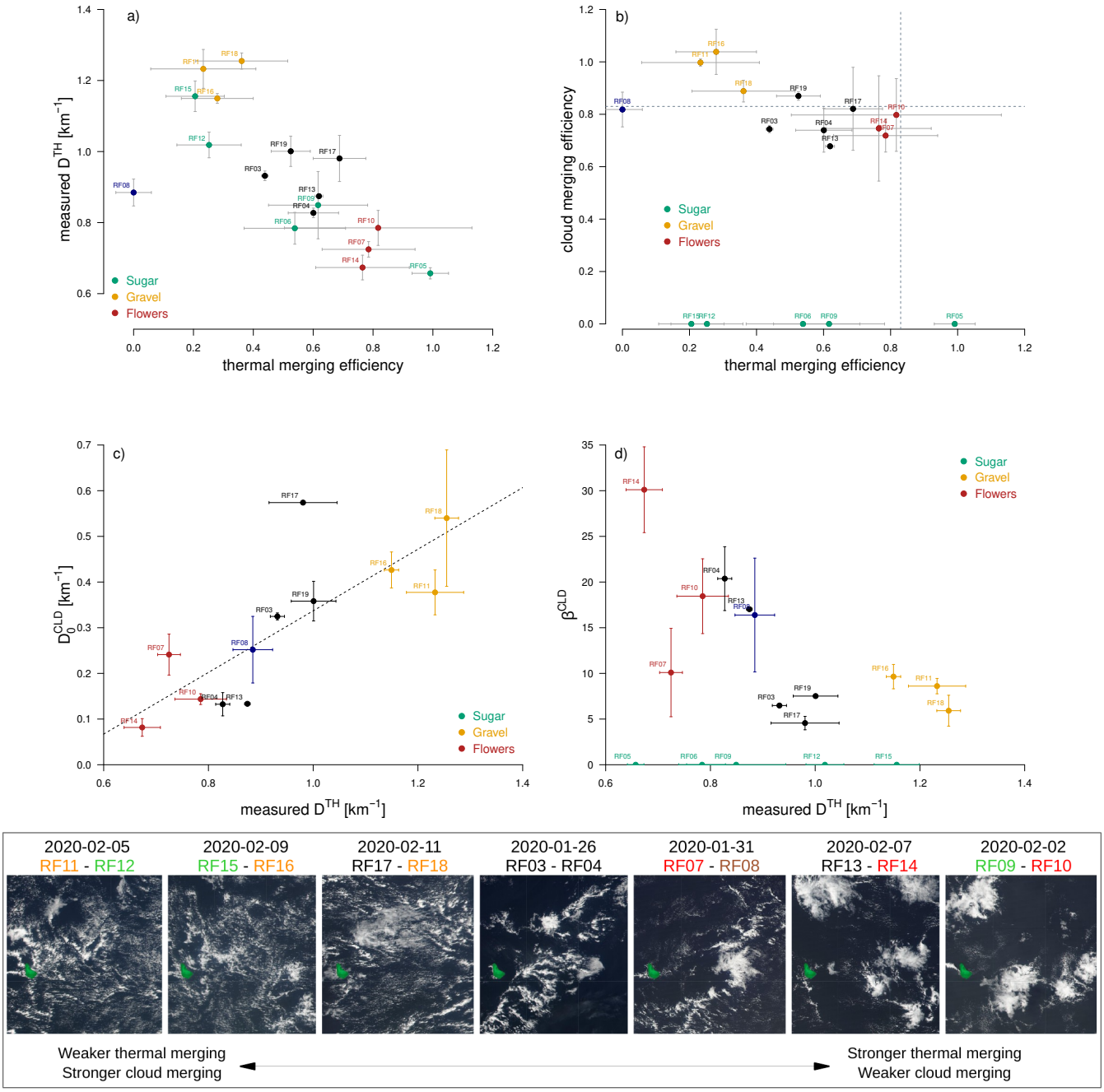


**Figure 12. From thermal merging to cloud patterns:** Relationship ~~between~~ (a) between thermal merging efficiency ~~(defined from thermal chord length distributions)~~ and thermal density $\mathcal{D}^{TH}$ (measured near cloud base) ~~and~~ , (b) between thermal merging efficiency and cloud merging efficiency around cloud base ~~(defined from~~ . The dashed line indicates the ~~thermal and cloud chord length distributions~~value of the critical merging efficiency (0.83). A few flights are highlighted, colored as a function of their prominent cloud mesoscale pattern (Sugar, ~~as well as~~ Gravel or Flowers). (c) and (d) show the ~~value of~~ relationships between the ~~critical~~ measured thermal density $\mathcal{D}^{TH}$ and the density of clouds before merging ~~efficiency (0.83)~~ $\mathcal{D}_0^{CLD}$ or the effective length of clouds $\beta^{CLD}$. (ebottom) For a few representative flights, illustration of the cloud mesoscale patterns in presence by Suomi-NPP satellite imagery snapshots (at 1:30 PM local time) over a domain (57$^o$-60$^o$ W, 12$^o$-15$^o$ N) encompassing the EUREC$^4$A field of operation (for each date, the corresponding flights are reported). The Barbados island (in

Fig. 12~~c~~ b suggests that the Gravel pattern corresponds to a minimized thermal merging but maximized cloud merging, and Flowers to a maximized thermal merging and minimal cloud merging. Therefore, when two cloud populations are present: the Gravel pattern maximizes cloud base widths (and in-cloud vertical velocities at cloud base) and thus the convective mass flux, while the Flower patterns minimizes the cloud base widths (and in-cloud vertical velocities) and the convective mass flux (Fig. 11c-d). It is consistent with the observation that the clouds embedded in the Gravel pattern are often deeper and associated with a higher rain rate than those embedded in Flowers (Schulz et al., 2021).

Fig. 12~~a shows~~ a-b show that the situations with only one cloud population (and thus no cloud merging by definition) occur for a wide range of thermal densities and merging efficiencies. The clouds that form in these cases are very small and shallow because they are rooted in small, unmerged thermals (section 6, Fig. 9b). In the absence of other cloud types (such as in RF06), this corresponds to a Sugar pattern (Stevens et al., 2020). However, even in the presence of other cloud types, such clouds are also found because merged and unmerged thermals often co-exist. Therefore, Sugar-like clouds are present in all cloud mesoscale patterns, albeit in a varying proportion that depends on the thermal merging efficiency. When the thermal merging efficiency increases, the effective factor of thermals increases more quickly than their own lengthscale (i. e. $\beta^{TH} \gg 1$, Fig. 8d). It makes the merging more and more efficient and thus the very shallow clouds more and more sparse. This explains why, in satellite images, the areas between the deepest clouds are less filled with very shallow clouds (and thus appear darker) in the case of Flowers (that are associated with strong thermal merging) than in the case of Gravel (Fig. 12c). It also explains why on a given day associated with a Flower pattern (e. g. on Feb 2, 2020), the ATR sampled one cloud population on one flight (RF09) when flying in-between the deep clouds, and two cloud populations on the other one (RF10) when flying across the deep clouds.

Interestingly, we note that the cloud merging efficiency of the different flights ($0.85 \pm 0.10$) is always close to 0.83 (only the Gravel patterns are associated with higher efficiencies). It means that the coupling between thermals and clouds is such that it maximizes the cloud density (section 5 and Fig. 6). Since the Gravel patterns are associated with a high thermal density but low cloud densities, they are more likely to evolve until the cloud density maximizes, while the Flower patterns (which are fed by wide and longer-lived thermals) are likely to be more stable and persistent. It is consistent with $\beta^{CLD}$, which increases with the lifetime of clouds and is larger for Flowers than for Gravel (Fig 12d).

Vertical and plan views of the interplay between thermals and clouds are represented schematically in Figures 10 and 13. The left-hand side of the cartoons correspond to a case of weak thermal merging (and thus high thermal density), and the right-hand side to a case of strong thermal merging and low thermal density. The two sides thus correspond to Gravel- and Flowers-types of mesoscale organization, taking into account that the very shallow clouds topping unmerged thermals (represented in the middle of Fig. 10 or around deep clouds in Fig. 13) are also part of these patterns. In the Flower case, deep clouds are represented with an extended cloud coverage at their top (a shallow anvil): it results from the water detrained from the convective core during the lifetime of the convective clouds, which can be particularly long in situations of strong thermal merging and large $\beta^{CLD}$ (Fig. 12d, section 6.2).

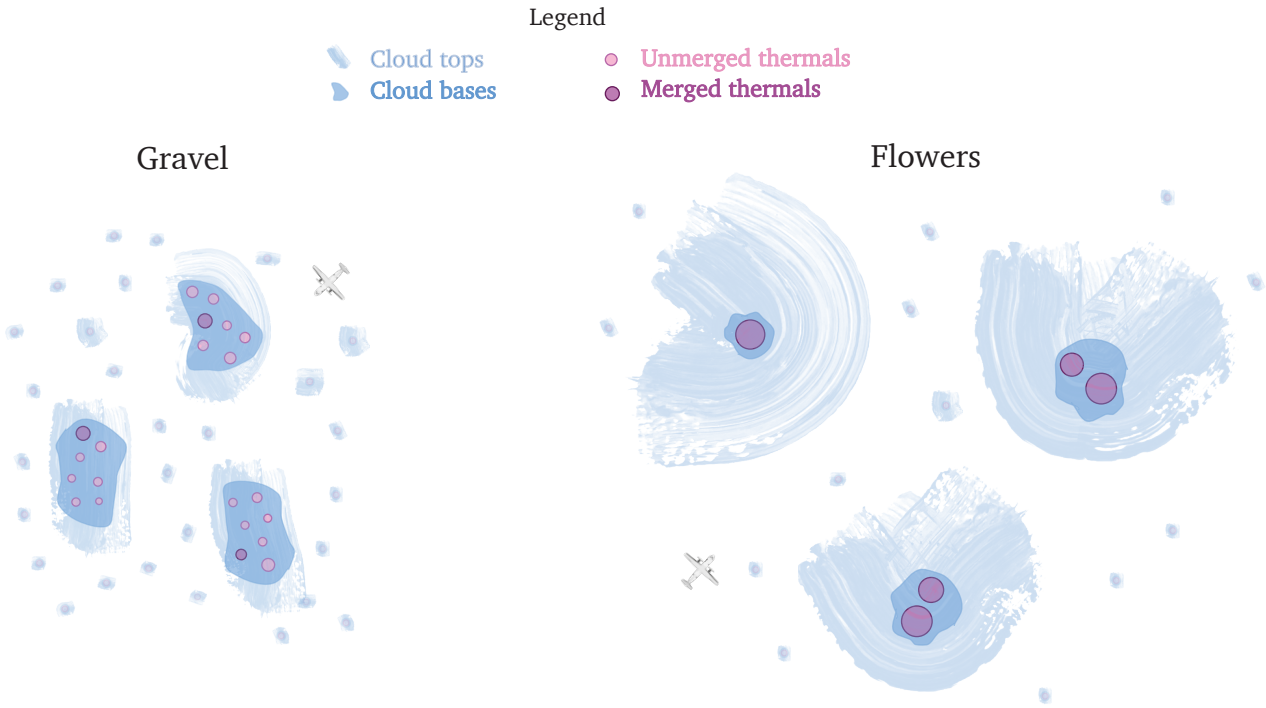


**Figure 13. The influence of merging on cloud mesoscale patterns (plan view).** When thermal merging is weak (left panel), there are few large thermals around cloud base (purple circles) and a high density of small unmerged thermals (pink circles); the clouds (in blue) that form at the top of the thermals thus merge efficiently, forming large cloud bases (dark blue) and leading to a strong mesoscale mass flux; this situation corresponds to the Gravel mesoscale pattern of cloudiness. When thermal merging is strong (right panel), the thermals widen but their density decreases, so that the thermals are more spaced: the clouds that form at the top of thermals are thus more isolated, which hinders cloud merging. Cloud bases are thus smaller than in the case of Gravel, and the mesoscale mass flux is weaker; on the other hand, clouds are fed by large (merged) thermals, which increases their lifetime and favors the formation of an extended cloudiness around cloud top; this situation corresponds to the Flower type of cloud mesoscale pattern.

### 7.3 Implications for the cloud fraction

The response of trade cumulus clouds to global warming has long been an important contributor to the uncertainty in low-cloud feedback and climate sensitivity (Bony and Dufresne, 2005; Vial et al., 2017). In climate models, this uncertainty is primarily related to changes in cloud fraction near the cloud base level (Brient et al., 2016). EUREC$^4$A observations allowed us to show that the climate models that predict the largest trade-cumulus feedbacks overestimate the cloud-base cloud fraction in the current climate, simulate a dependence of this cloud fraction on convection that is at odds with observations, and exhibit difficulties in simulating daily transitions between shallow and deeper trade cumuli (Vogel et al., 2022; Vial et al., 2023). This calls for investigating the influence of the merging process on the cloud fraction near cloud base.

As discussed in section 5, the final coverage of merging objects depends on their merging efficiency and $\beta$. According to equation 12, the coverage increases as the initial density $\mathcal{D}_0$ or size $L_0$ increases, but it is bounded by the maximum value $f_{max} = 1/\beta$. Therefore, for a given merging efficiency, the final coverage decreases as $\beta$ increases. During EUREC$^4$A, $\beta^{CLD} \geq 5$ (Figure 12d) and therefore 0.2 appears to be an upper bound for the cloud fraction around cloud base. Furthermore, since $\beta \mathcal{D}_0 L_0^{CLD}$ is never far from 0.83 (Figure 12b), the cloud base cloud fraction is well approximated by $(1 - e^{-0.83})/\beta^{CLD}$ (Figure 14a). It highlights the important role of $\beta^{CLD}$ in modulating, and limiting, the cloud fraction around cloud base.

As discussed in section 6.2 and Appendix A, simple physical arguments suggest that $\beta$ encapsulates the influence that the circulation produced by convective objects exerts on neighbouring objects. ~~This influence~~ Then, how to physically interpret the fact that $\beta^{CLD}$ constrains the cloud fraction? The $f_{max}$ limit corresponds to the maximum cloud fraction for which the clouds' basins of attraction remain non-overlapping. In a cloud field with an area fraction $1/\beta^{CLD}$, then any new clouds born in the domain would necessarily be within an existing cloud's "basin of attraction" and would therefore merge with that cloud (in the simplest case where $\beta^{CLD} = 1$, a new cloud born in a region with a cloud fraction of unity would necessarily imply overlap and merging with existing clouds and no further increase in cloud fraction). Another interpretation is that the circulation induced by clouds likely promotes a mass convergence around their base level that favors the merging of thermals and thus decreases the cloud base fraction (Fig. 10).

Moreover, the circulation induced by clouds facilitates the merging process ~~,~~ all the more that the ~~objects~~ clouds live longer. How may thermal merging influence the cloud lifetime? When thermal merging increases, the thermals become wider, and therefore they are more likely associated with positive buoyancy and stronger vertical velocities (Böing et al., 2012; Rochetin et al., 2014; Morrison et al., 2022), and thus with stronger circulations. Clouds are likely to live longer when they are fed by such active thermals, and therefore associated with a larger $\beta^{CLD}$.

Consistently, the situations with weak thermal merging, that predominantly correspond to the Gravel type of organization (section 7.2), are associated with short-lived clouds, $\beta^{CLD}$ values ranging from 6 to 10 and a measured cloud fraction that ranges from 0.07 to 0.1 at cloud base. In contrast, the situations with strong thermal merging, that correspond to Flowers, embbed clouds that have much longer lifetimes (as shown by Narenpitak et al. (2021), on 2020-02-02 the cloud flowers followed along their Lagrangian trajectory seemed almost motionless for more than 12 hours), $\beta^{CLD}$ ranges from 10 to 30 and

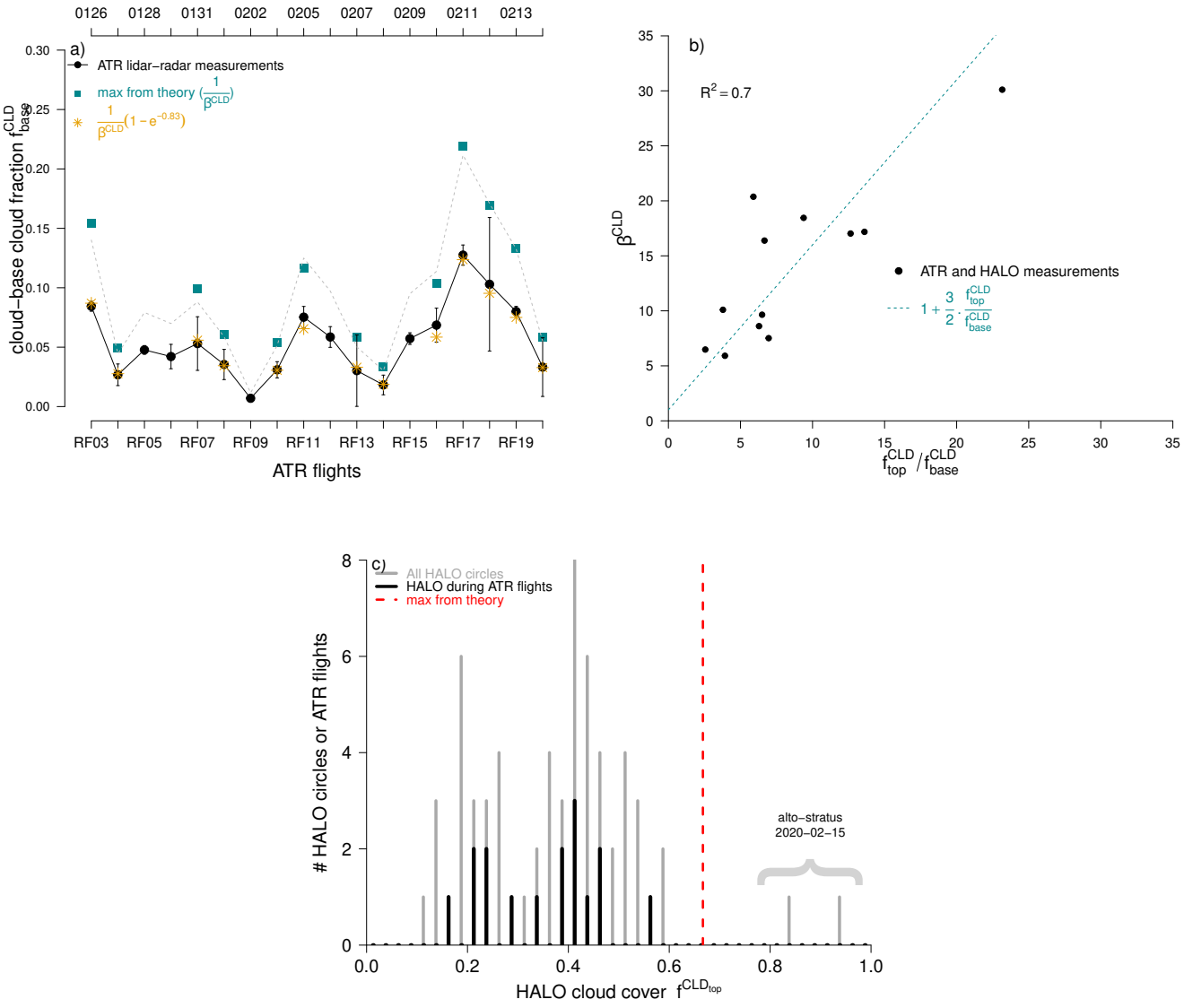


**Figure 14. Implications of merging for the cloud fraction at cloud base and cloud top.** (a) Evolution of the cloud-base cloud fraction measured from the ATR using horizontal lidar-radar remote sensing (in black, from Bony et al. (2022)). Also reported is the maximum cloud fraction predicted by the merging theory ($1/\beta^{CLD}$, only available when two cloud populations are present) and the cloud fraction estimated from theory when assuming $(\beta \mathcal{D}_0 L_0)^{CLD} = 0.83$. (b) Relationship between $\beta^{CLD}$ (inferred from cloud-base measurements as explained in section 5) and the ratio between the cloud cover measured from above by HALO ($f_{top}^{CLD}$ and the cloud fraction measured at cloud base by the ATR ($f_{base}^{CLD}$). (c) Histogram of the cloud cover measured from the upper troposphere by HALO using downward-looking lidar-radar remote sensing and radiometers. Data from all HALO circles performed during EUREC$^4$A are shown in grey (from Konow et al. (2021). HALO measurements performed during the ATR flights are shown in black. The red line shows the upper bound (2/3) on $f_{top}^{CLD}$ estimated from theory. The only measurements exceeding this value were made on Feb 15th 2020, when HALO was flying above a persistent layer of altostratus independent of boundary-layer processes.

the cloud base cloud fraction does not exceed 0.05. By enhancing the lifetime of clouds, thermal merging thus exerts a strong control on the cloud-base cloud fraction.

As explained in ~~Appendix A~~section 6.2, $\beta^{CLD}$ can also be related to the aspect ratio of clouds, i.e. the ratio between cloud length scales at cloud top and at cloud base: ~~$\beta = 1 + \frac{\gamma}{2}\frac{f_{top}^{CLD}}{f_{base}^{CLD}}$~~ $\beta = 1 + \gamma\frac{f_{top}^{CLD}}{f_{base}^{CLD}}$, where $\gamma = h'/h$ is the ratio between the outflow and inflow layer depths of the air transported by the cloud circulation. Since $f_{base}^{CLD}$ is bounded by $1/\beta^{CLD}$, the cloud cover measured from top is also bounded by ~~$\frac{2}{\gamma}(1 - 1/\beta^{CLD})$~~ $\frac{1}{\gamma}(1 - 1/\beta^{CLD})$. Figure 14b shows the relationship between $\beta^{CLD}$ (inferred from ATR measurements as explained in section 5) and the ratio $\frac{f_{top}^{CLD}}{f_{base}^{CLD}}$, using $f_{top}^{CLD}$ measurements from the downward-looking instruments on board HALO (Konow et al., 2021).

Indeed, the two quantities are actually strongly correlated (Pearson correlation equals 0.84), and the relationship is reasonably reproduced using $\gamma$ = 3/2, supporting our hypothesis that the effective factor $\beta^{CLD}$ arises from the presence of cloud-induced circulations. We thus expect $f_{top}^{CLD}$ to be bounded by ~~2~~1/$\gamma$ = 2/3. The histogram of $f_{top}^{CLD}$ values inferred from HALO measurements (considering the maximum cloud fraction estimates across the different instruments) during the whole EUREC$^4$A field campaign shows that this value actually represents an upper bound for the measurements (Fig. 14c). Over the 86 circles flown by HALO during ~~Jan-Fev~~ Jan-Feb 2020, the cloud fraction exceeded this value only twice, on 2020-02-15, when HALO was flying above a persistent layer of altostratus that has no reason to depend on boundary layer processes and thermal merging.

## 8 Conclusion and discussion

In line with early studies of atmospheric convection (Simpson et al., 1965; Ooyama, 1971; Arakawa and Schubert, 1974; LeMone and Pennell, 1976; Lenschow and Stephens, 1980; Williams and Hacker, 1993), this study emphasizes the importance of the thermal-cloud interplay in convection dynamics, and confirms its imprint on the statistical distribution of cloud-base widths. It goes further by demonstrating the central role of the merging process in facilitating this interplay and the constraints it imposes on the mesoscale organization of convection ~~.~~and the cloud fraction.

### 8.1 Summary of main findings

These findings are the result of analyzing and interpreting the interplay between thermals, clouds, mesoscale circulations and cloud patterns that was observed over the tropical Atlantic Ocean during the EUREC$^4$A field campaign. During the campaign, the atmosphere was statistically sampled over a four-week period with two research aircraft that followed a repeated flight pattern. The ATR aircraft flying in the lower troposphere characterized boundary-layer thermal and cloud base chords using high-frequency humidity measurements and horizontal lidar-radar remote sensing while the HALO aircraft observed clouds from above and measured mesoscale circulations using dropsondes.

Airborne observations taken at several heights throughout the subcloud layer show that the density of thermal chords decreases with height while their average size increases. The observations also reveal that the distribution of thermal chord lengths is exponential in the surface layer, and that it is well fitted by a sum of two exponential functions higher up in the subcloud

layer and near cloud base. Measurements of cloud chord lengths around the cloud base level also exhibit two populations of chords. Similar to thermals, the size distribution of cloud chords is well fitted by a sum of two exponentials, when considering either the whole campaign or individual flights. The length scale of the first cloud exponential is similar to the average size of individual thermals, while the length scale of the second cloud exponential is several times larger. Then, the detailed analysis and interpretation of these observations addresses three main questions : 1) What physical process explains the double exponential distributions? 2) How do the thermal and cloud size distributions relate to each other? 3) How do these distributions inform our physical understanding of the mesoscale organanization of convection?

Physical insight and mathematical calculations, supported by simple statistical simulations, show that the merging of objects with initially exponentially distributed chord lengths leads to a sum of two exponential distributions. One exponential corresponds to objects that have merged, and the other corresponds to objects that have not yet merged. Furthermore, physical arguments suggest that the circulation created by convective objects influences the surrounding objects in a way that facilitates the merging process. This influence is formally similar to assuming that the objects have an effective length greater (by a factor $\beta$, the effective factor) than their actual length. The merging efficiency and effective factor of objects can be inferred from their chord length distribution and total coverage after merging.

Based on this conceptual framework, we diagnose the merging efficiency and effective factor of thermals and clouds using EUREC$^4$A observations, and we predict the thermal density that results from the merging process. The good agreement between this prediction and the measured thermal density (which was not used to infer the merging diagnostics) provides an independent test of the consistency between the theory and the observations. We then analyze the ensemble of EUREC$^4$A observations in the light of this interpretation framework.

This analysis suggests that the thermals formed in the surface layer progressively merge as they rise through the subcloud layer. This decreases the thermal density and creates two populations: one of small, unmerged thermals averaging 100-120 m, and another of larger thermals averaging about 300 m. The cloud chord length distributions are closely related to these thermal populations (Fig. 10). Merged and unmerged thermals constitute the roots of cloud-base widths~~that also merge and form~~ : upon reaching the LCL, they saturate and give rise to cloud shoots (incipient cloud bases) which in turn merge and produce two cloud populations. The clouds that ~~do not merge~~ results from unmerged cloud shoots are horizontally small (they have roughly the same size as individual thermals), very shallow and non drizzling. On the other hand, the clouds that ~~merge are rooted in merged thermals; they~~ result from merged cloud shoots have a wider base, develop deeper and produce drizzle. The circulation they create around them (encapsulated by the effective factor) is also stronger, which likely reinforces the concentration and merging of underlying thermals, and reduces the presence of very shallow clouds in their vicinity. The interplay between thermals and clouds, combined with the merging process, has several significant implications.

First, the merging efficiencies of thermals and clouds are negatively correlated: when thermal merging is weak, the thermal density is high, which results in a high density of ~~cloud-base roots~~cloud shoots. This facilitates cloud merging, forms large cloud bases, increases the mesoscale mass flux and strengthens mesoscale circulations. However, the convergence of thermals below large clouds eventually strengthens thermal merging, which produces wider but more isolated thermals and a lower density of ~~cloud-base roots~~cloud shoots. This hinders cloud merging and reduces the mesoscale mass flux. The interplay between thermal

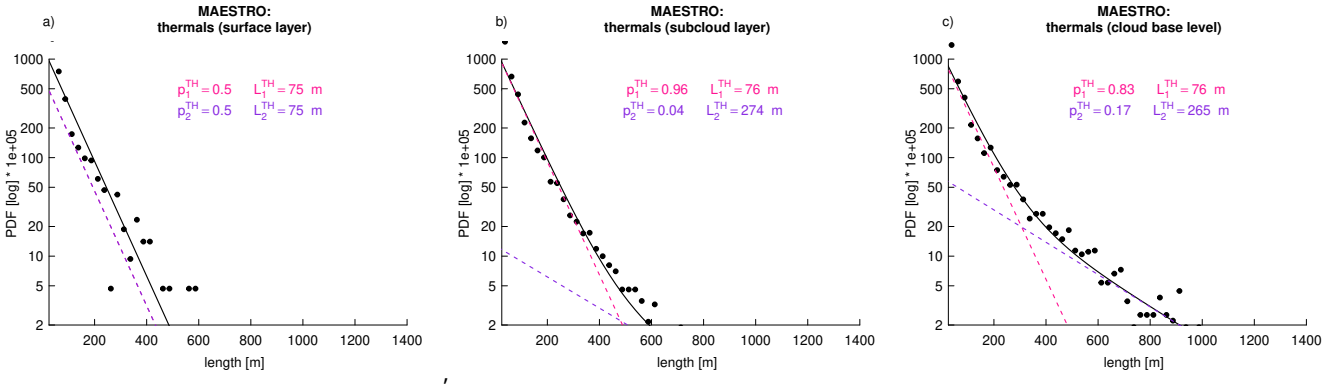


**Figure 15. Universality of the thermal chord distributions?** Same as Figure 1 but for measurements from the *Mesoscale Organisation of Tropical Convection* (MAESTRO) field campaign that took place on Aug-Sept 2024 around Cape Verde in regimes of shallow to deep convection.

and cloud merging thus represents a negative feedback on the growth of mesoscale circulations, thus regulating the intrinsically unstable growth of shallow mesoscale circulations (Janssens et al., 2023).

Second, we observe a correspondence between the degree of thermal merging and the type of prominent mesoscale cloud pattern: situations of weak thermal merging tend to be associated with Gravel-type organization, while situations of strong thermal merging tend to be associated with Flower patterns. On the other hand, the very shallow clouds that cap single thermals can be found in all situations, either alone (thus forming a Sugar-type organization) or in association with other cloud types. Moreover, since ~~thermal~~ cloud merging promotes the formation of larger cloud bases, deeper clouds and stronger mass fluxes, it contributes to the development of the shallow mesoscale circulations that have been shown to accompany the transitions from Sugar-Gravel to Flower types of organization in Large-Eddy Simulations (Narenpitak et al., 2021). The analysis of these simulations, that will be presented in a separate paper, confirms this inferrence (Maury et al., in preparation).

Finally, physical arguments suggest that the maximum cloud fraction that can be achieved at cloud base is inversely proportional to the cloud effective factor, which depends on the cloud lifetime. Since clouds presumably live longer when they are fed by wide, isolated thermals than when they are fed by small thermals, thermal merging reduces the cloud fraction near cloud base. This is consistent with the minimal cloud fraction measured at cloud base in Flower-type organizations, and with the positive relationship between cloud fraction and mesoscale mass flux pointed out by Vogel et al. (2022). Physical arguments also suggest that the cloud top coverage is limited by the lifetime of clouds, and EUREC$^4$A measurements are consistent with this suggestion.

### 8.2 Open questions and perspectives

A number of observed features remain to be interpreted. For instance, a surprising observation is that the cloud merging efficiency is never far from 0.83 (Fig. 12b), which is the theoretical value that maximizes the cloud density after merging

(Fig. 6). Whether or not this is a general feature constrained by some physical process remains to be understood. Another interesting feature is the underestimate, compared to observations, of the thermal density predicted by theory in situations of maximal thermal merging or minimal thermal density after merging (Fig. 8a). This discrepancy suggests the influence of additional processes in the control of the thermal density. These processes might include the influence of mesoscale circulations, which concentrate thermals in ascending branches (as shown by Fig. 11b at the scale of a 200 km circle), ~~the influence of smaller-scale circulations created by clouds~~ or the presence of cold pools, which may concentrate thermals and thus favor thermal merging at their edge. The discrepancy may also result from the mass convergence induced by clouds in the subcloud layer, which may ~~not be~~ influence the distribution of thermals beneath clouds and thus thermal merging but is not adequately accounted for by the effective factor ~~and may influence the distribution of thermals beneath clouds, or the presence of cold pools~~of thermals (because it arises from clouds). These influences will need to be studied. Finally, the sensitivity of thermal merging to factors such as the ~~mass convergence in the subcloud layer, the~~ strength of surface turbulent fluxes, the Bowen ratio or environmental conditions, and the sensitivity of cloud merging to humidity and wind shear will have to be investigated.

More importantly, this study emphasizes the role of thermal- and cloud-induced circulations in shaping mesoscale organization and cloud patterns. Within the analysis framework presented here, these circulations are conceptualized by the effective factor $\beta$, which quantifies the basin of attraction exerted by a convective object on its surroundings and influences the merging process as if convective objects had an effective size $\beta$ times their actual size. The factors that influence $\beta$ remain to be clarified. For instance, how should we interpret the fact that inter-flight variability of $\beta^{TH}$ is larger than its intra-flight variability (Figure 8d)? A deeper investigation into the dependence of $\beta$ on convective object properties and environmental conditions would help answer this question. In addition, this study demonstrates the role of merging in shaping the size distribution of thermals and clouds, but does not show how exactly the merging – or the contact between two adjacent objects – actually occurs. The influence on the size, orientation and movement of rising thermals and clouds, and consequently on merging efficiency, of processes such as entrainment at thermal and cloud edges, ambient horizontal flow or wind shear, or buoyancy-induced pressure gradients, should be further investigated with additional observations and/or simulations.

The findings of this study offer new opportunities to understand and predict the mesoscale organization of convection, as well as its role in climate.

Given the importance of the transition between shallow and deeper trade cumuli in cloud feedback (Vial et al., 2023), and the uncertainty surrounding the role of cloud mesoscale organization in climate sensitivity (Bony et al., 2015; Nuijens and Siebesma, 2019; Becker and Wing, 2020; Alinaghi et al., 2024), it will be important to verify that the models used to study convective organization and cloud feedbacks realistically represent this essential piece of atmospheric physics. By relating the statistical distribution of thermal and cloud chords to the processes that control the cloud's geometry, convective mass fluxes and mesoscale circulations, this study paves the way towards a better interpretation of the ability of numerical models to predict the different forms of mesoscale convective organization: Why do Large Eddy Simulation (LES) models or Cloud Resolving Models exhibit more success or difficulty predicting Flower-type of organization than Gravel? Why do they predict clouds that may be too scattered or on the contrary excessively wide, deep and clustered? How does the representation of thermal merging and the thermal-cloud interplay depend on the spatial resolution of models? These questions may be addressed through model

inter-comparisons such as EUREC$^4$A-MIP (https://eurec4a.eu/mip) or large ensembles of simulations such as the Cloud Botany dataset (Jansson et al., 2023). Analyzing these simulations would also allow us to investigate how environmental conditions influence thermal merging, which will advance understanding of how the mesoscale convective organization might respond to climate change.

In turn, the conceptualization of thermal and cloud populations as a mixture of two populations that interact and evolve through merging could help develop conceptual models that aim at representing the spectrum of cumulus clouds, their dynamics and their mesoscale organization. Such conceptual models could also be used to parameterize the mesoscale organization of convection in coarse general circulation models. With the exception of Rochetin et al. (2014), pioneering studies in this direction have often described the statistical distribution of cloud base widths using power laws or other heavy-tail distribution functions (Sakradzija et al., 2015; Neggers, 2015; Neggers and Griewank, 2022). Studies also noticed the frequent presence of a scale break dependent on the spatial organization of convection (e. g., Neggers and Griewank (2022)), and Savre and Craig (2023) suggested that the merging of cloud cores could influence the scale behavior of the cloud size distributions. The mathematical arguments presented in section 5 suggest that a double exponential would be a more natural description of these distributions. It will need to be confirmed.

Finally, since EUREC$^4$A took place in a regime of shallow convection, the question arises as to whether the findings of this study are specific to shallow convection, or could apply to a broader range of convective regimes. Exponential distributions of updraft chord lengths and mass fluxes have been pointed out in various contexts, ranging from observations of cloud-free continental convection (Miao et al., 2006) to idealized simulations of deep convection (Cohen and Craig, 2006). It remains to be clarified whether the absence of a second exponential may be due to the absence of merging (as may occur in simulations without mesoscale organization), and/or to a spatial resolution of simulations or observations that is too coarse to detect the smallest thermals or clouds. In any event, several elements suggest a certain universality of our results. First, the mathematical calculations and simple statistical simulations presented in section 5 are not specific to shallow convection and would apply equally to deep convection. Second, the interplay between thermals and clouds that has been characterized here for different organizations of shallow clouds resembles that at work during the transition from shallow to deep convection over land or ocean (Grabowski et al., 2006; Kuang and Bretherton, 2006; Böing et al., 2012; Rochetin et al., 2014; Morrison et al., 2022), including in the presence of mesoscale circulations (Rousseau-Rizzi et al., 2017). However, this important question deserves further investigation.

Another question to be addressed is how much the merging process contributes to the self-organization of convection. Modelling studies suggest that cold pools or radiatively-driven circulations are not necessary to organize shallow convection (Bretherton and Blossey, 2017; Janssens et al., 2023), and this is consistent with our results. Whether the merging process can also lead to the spontaneous organization of deep convection, and should be added to the list of physical processes that have already been identified (Muller et al., 2022), will have to be explored.

The recent MAESTRO (*Mesoscale organisation of tropical convection*, https://maestro.aeris-data.fr) field campaign, which took place in August-September 2024 near Cape Verde as part of ORCESTRA (*Organized Convection and EarthCARE Studies over the Tropical Atlantic*, https://orcestra-campaign.org), is an opportunity to explore the universality of the merging process

across convective regimes. During MAESTRO, the ATR measured again humidity at a fast rate at different levels of the subcloud layer and at cloud base, in a wide range of meteorological situations ranging from shallow to deep convection ~~(Jaffeux et al., submitted)~~(Jaffeux and Lothon, 2025; Jaffeux et al., submitted). Using the same methodology as described in section 3, we analyzed the thermals sampled during this campaign. Figure 15 shows that the thermal chord length distributions derived from MAESTRO observations resemble those from EUREC$^4$A, further supporting the idea of a certain universality in the processes revealed by EUREC$^4$A observations. However, further studies will be needed to confirm this conclusion, and to investigate how the interplay between thermal, clouds and circulations varies across a large diversity of convective organizations.

Finally, this study emphasizes the importance of considering the circulations induced by convective objects to understand the mesoscale organization of convection. This insight harkens back to a school of thought considering convective objects not just as thermodynamic entities (e. g. Arakawa and Schubert (1974)) but also as geometric and dynamic entities (e. g. Bretherton (1987); Neggers (2015); Poujol (2025)). As fine-scale atmospheric models are now being used on large domains and multi-scale observations of convection, such as those from EUREC$^4$A or ORCESTRA, are becoming available, a more complete understanding of the dynamical nature of thermal and clouds, and its implications for mesoscale oganization, is not only becoming warranted, but also possible.

*Data availability.* All data used in this study are published in the EUREC$^4$A database of AERIS (https://eurec4a.aeris-data.fr/). It includes: the BASTALIAS dataset of horizontal lidar-radar measurements ((Delanoë et al., 2021), https://doi.org/10.25326/316, presented in Bony et al. (2022)), fast measurements of water vapor, which are part of the turbulence dataset (version 1.9 of Lothon and Brilouet (2020), https://doi.org/10.25326/128, presented in Brilouet et al. (2021)), dropsondes measurements of mass divergence and vertical velocity (v2.0.0 of the JOANNE dropsonde dataset, https://doi.org/10.25326/246, presented in George et al. (2021)), and estimates of the convective mass flux at cloud base (presented in Vogel et al. (2022)). The MAESTRO turbulence data used in this study are derived from SAFIRE in situ measurements available on AERIS (Bony and SAFIRE, 2024; Jaffeux and Lothon, 2025).

## Appendix A: Effective length of convective objects

In this section, we aim at providing an explanation for the merging process of convective objects, and deriving a simple merging criterion based on basic properties of the convective objects.

Let us consider two updrafts, such as clouds or thermals. ~~We could consider that two updrafts merge if, and only if,~~ These updrafts can merge if they touch each other, as ~~it is represented on figure A1~~represented in Figure A1a. However, ~~this view is partly erroneous.~~

~~Indeed, we can assume that updrafts will interact with each other through the circulation that they create. If two updrafts do not touch but~~ we can also consider that if the updrafts are close enough, they ~~will attract each other and eventually merge.~~can merge by attracting each other through the circulations they create (Fig. A1b). This process is illustrated on ~~figure A2, where the circulation of two updrafts and their resultant is shown.~~ Figure A2, that sketches the resulting circulation implied by two

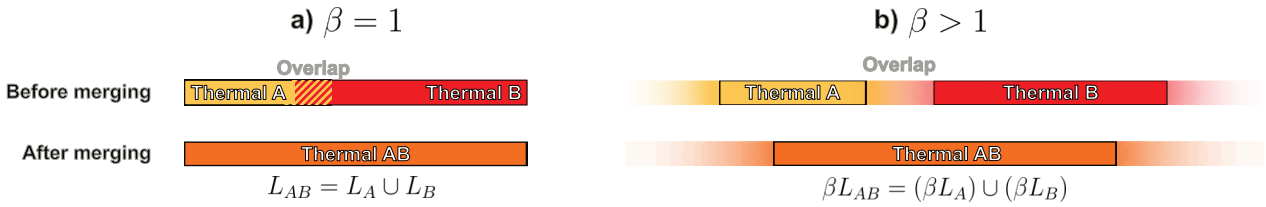


**Figure A1.** Illustration of the merging process assuming two objects merge (a) if and only if they overlap or (b) if their *basins of attraction* overlap – the basin of attraction (or effective length) of object A has a length $\beta L_A$, where $L_A$ is the actual length of object A and $\beta$ is the effective factor (shown in shading, defined in Appendix A and further interpreted in section 6.2). The rules for object merging are as follows. When $\beta = 1$, the length of the merged ($L_{AB}$) object will be the union of the two incipient objects' lengths ($L_A \cup L_B$). When $\beta > 1$, the length of the merged object's basin of attraction ($\beta L_{AB}$) will be the union of the two incipient objects' basins of attraction ($\beta L_a \cup \beta L_B$).

convective objects, at the moment the objects are created. Assuming that the position of the updrafts is controlled by their base (where the warm bubbles are formed), the two updrafts attract each other as indicated by the red arrows. To account for this process, let us note by $T_{life}$ the lifetime of ~~a~~ an updraft. Two updrafts will merge if they have the time to attract each other until merging before they die.

We aim at computing the time needed for two updrafts to merge. We first consider an updraft (updraft ~~1~~A; in blue on the schematic) that has a depth $H$, a width ~~$L_1$~~$L_A$, and a vertical velocity ~~$w_1$~~$w_A$. The horizontal wind ~~$u_1$~~ $u_A$ created by updraft ~~1~~ A can be computed by mass conservation~~: assuming~~ . Assuming that the updraft is fed by an inflow layer of depth $h$ then mass conservation ~~writes:~~

$$w_1 L_1 = 2 u_1 h$$

implies that $w_A L_A = 2 u_A h$, which directly provides an estimate for ~~$u_1$~~$u_A$. Let us now consider a second updraft (updraft ~~2~~B) that is located at a distance $\ell$ from updraft ~~1.~~ A. We first assume that updraft ~~2~~ B is passive for simplicity. The time necessary for two updrafts to merge is given by:

$$T_{merge}(\ell) = \frac{\ell}{u_1} \frac{\ell}{u_A} = 2 \frac{h\ell}{w_1 L_1} \frac{h\ell}{w_A L_A} \tag{A1}$$

To improve the physical interpretation of the expression, we define the transit time of the updraft:

$$T_{transit} = \frac{H}{w_1} \frac{H}{w_A} \tag{A2}$$

which is the time necessary for an air parcel to travel from the bottom to the top of the updraft.

The merging will occur if, and only if, $T_{merge} \leq T_{life}$. This translates into a maximum distance between the edges of the two updrafts for merging to occur:

$$\ell_{max,1} \ell_{max,A} = \frac{L_1}{2} \frac{L_A}{2} \frac{H}{h} \frac{T_{life}}{T_{transit}} \tag{A3}$$

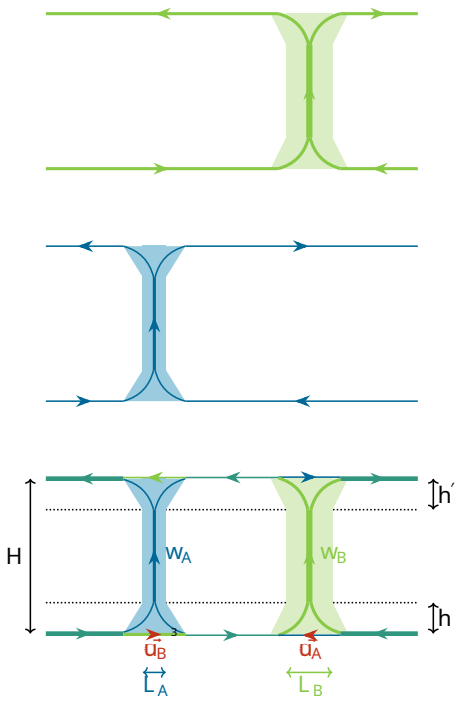


**Figure A2.** The circulation created by two updrafts, as well as the resulting circulation. The red arrows highlight the advection experienced by the base of each updraft, and indicate the attraction between the two updrafts. H, $h$ and $h'$ are the depths of the updraft and of the inflow and outflow layers, respectively. ~~$u_1$~~ $u_A$ and ~~$u_2$~~ $u_B$ are the horizontal winds induced by updrafts ~~1~~ A and ~~2~~B, respectively.

Up to this point, we have considered that updraft ~~2~~ B was passive. However, it also exerts an attracting force on updraft ~~1~~ A and the real maximal distance for the merging between the two updrafts is given by:

$$\ell_{max,1+2 max,A+B} = \ell_{max,1 max,A} + \ell_{max,2 max,B} = \frac{L_1 + L_2}{2} \frac{L_A + L_B}{2} \frac{H}{h} \frac{T_{life}}{T_{transit}} \tag{A4}$$

~~Considering this extra distance between the two updrafts for merging to occur is straightforward, because it happens that this distance is proportional to the size of the updrafts. Therefore, it is formally analog to consider a situation in which the actual updrafts are replaced by analog objects that have their size increased by $\ell_{max}$ on either side. In other words, the effective size of the updraft corresponds to it actual size,~~ and therefore merging will occur if the *centers* of the two updrafts are separated by less than:

$$\frac{L_A + L_B}{2} + \ell_{max,A+B} = \frac{L_A + L_B}{2} \left(1 + \frac{H}{h} \frac{T_{life}}{T_{transit}}\right). \tag{A5}$$

Then, everything happens as if the updrafts need to overlap to merge, but having a length multiplied by an effective factor ~~:~~ $\beta$ :

$$\beta = 1 + \frac{1}{2}\frac{H}{h}\frac{T_{life}}{T_{transit}} \tag{A6}$$

~~There are several other interpretations of $\beta$. Indeed, $T_{life}/T_{transit}$ can be viewed as the number of successive warm bubbles that rise over the course of the life of an updraft, $N_{bubbles}$.~~

~~For clouds,~~ In other words, taking into account the influence of the thermal-induced circulations on merging amounts to replace the actual updrafts by effective objects whose size is the actual size of the updrafts multipled by $\beta$ ~~can also be expressed in terms of the ratio between the area of the anvil of the cloud and its core size. Indeed, the cloud core size is $L_{core} = L_1$, while the cloud anvil size is $L_{anvil} = 2u_1T_{life}$. Therefore we get:~~

$$\frac{L_{anvil}}{L_{core}} = \frac{2u_1T_{life}}{L_1} = \frac{H}{h'}\frac{T_{life}}{T_{transit}}$$

~~where $h'$ is the depth of the outflow layer at the cloud top~~.

~~In other words, $\beta$ is directly related to the (aspect) ratio between the size of the anvil and the size of the core of a cloud:~~

$$\begin{aligned}\beta &= 1 + \tfrac{1}{2}\tfrac{H}{h}\tfrac{T_{life}}{T_{transit}} \\ &= 1 + \tfrac{1}{2}\tfrac{H}{h}N_{bubbles} \\ &= 1 + \tfrac{1}{2}\tfrac{h'}{h}\tfrac{L_{anvil}}{L_{core}}\end{aligned}$$

The effective updrafts have their size multiplied by $\beta$, and they merge if and only if they actually touch. As a result, we can consider a population of effective updrafts, that have a characteristic size $\beta L_0$ and a density $\mathcal{D}_0$, and we want to study the efficiency of the merging process between those effective updrafts. The merging between those effective updrafts acts as shown on ~~figure~~ Figure A1. After merging, it ~~will be~~ is straightforward to come back to the size distribution of real updrafts, by dividing again the size of the effective updrafts by the factor $\beta$.

~~Because the life time of an updraft is usually at least as long as the transit time, $\beta$ is always larger than 1, and is typically of a few units. It can reach much larger values for updrafts that can live a very long time, that typically produce extensive anvil clouds as it is the case for flowers.~~

*Author contributions.* SB designed the study, analyzed all data and wrote the paper. The first four authors jointly interpreted the results and discussed their implications. BP designed and carried out the mathematical calculations and conceptualized the effective factor. BMK and JW designed and ran the simple statistical simulations. SB, ML and JD led the ATR operations of the EUREC$^4$A and MAESTRO campaigns. All other authors contributed to the collection, the processing or the interpretation of observations. All co-authors edited the manuscript.

*Competing interests.* None

*Disclaimer.* Part of this work (section 5.1, Appendix A) was presented in the PhD thesis of Basile Poujol (Sorbonne University, 2025).

*Acknowledgements.* We thank all the scientists, especially Bjorn Stevens, engineers, technicians, pilots and administrative people from Safire, LATMOS, LSCE, LAMP, LAERO, LMD, MPI, DLR, CIMH and INMG who made the EUREC$^4$A and MAESTRO field campaigns possible. Safire, the French facility for airborne research, is an infrastructure of the French National Center for Scientific Research (CNRS), Météo-France and the French National Center for Space Studies (CNES). We thank Julius Mex and Theresa Mieslinger for their help during the course of this study. This research received funding from ERC (EUREC4A grant no. 694768 and MAESTRO grant no. 101098063), H2020 (NextGEMS grant no 101003470), CNES (EMC-Sat grant and post-doctorate grant fellowship) and ESA (contract no. 281042). The Ecole Normale Supérieure is acknowledged for funding BP's PhD fellowship and JW's visit at LMD. We sincerely thank the two anonymous reviewers for their careful and thoughtful reviews, which substantially contributed to sharpening the arguments and improving the clarity of this study.

## References


Agee, E.: Mesoscale cellular convection over the oceans, Dynamics of Atmospheres and Oceans, 10, 317–341, https://doi.org/https://doi.org/10.1016/0377-0265(87)90023-6, 1987.

Albright, A. L., Bony, S., Stevens, B., and Vogel, R.: Observed Subcloud-Layer Moisture and Heat Budgets in the Trades, Journal of the Atmospheric Sciences, 79, 2363 – 2385, https://doi.org/10.1175/JAS-D-21-0337.1, 2022.

Albright, A. L., Stevens, B., Bony, S., and Vogel, R.: A New Conceptual Picture of the Trade Wind Transition Layer, Journal of the Atmospheric Sciences, 80, 1547 – 1563, https://doi.org/10.1175/JAS-D-22-0184.1, 2023.

Alinaghi, P., Janssens, M., Choudhury, G., Goren, T., Siebesma, A. P., and Glassmeier, F.: Shallow cumulus cloud fields are optically thicker when they are more clustered, Quarterly Journal of the Royal Meteorological Society, 150, 3566–3577, https://doi.org/https://doi.org/10.1002/qj.4783, 2024.

Arakawa, A. and Schubert, W. H.: Interaction of a Cumulus Cloud Ensemble with the Large-Scale Environment, Part I, Journal of Atmospheric Sciences, 31, 674 – 701, https://doi.org/https://doi.org/10.1175/1520-0469(1974)031<0674:IOACCE>2.0.CO;2, 1974.

Asai, T. and Kasahara, A.: A Theoretical Study of the Compensating Downward Motions Associated with Cumulus Clouds, Journal of Atmospheric Sciences, 24, 487 – 496, https://doi.org/https://doi.org/10.1175/1520-0469(1967)024<0487:ATSOTC>2.0.CO;2, 1967.

Batchelor, G. K.: Heat convection and buoyancy effects in fluids, Quarterly Journal of the Royal Meteorological Society, 80, 339–358, https://doi.org/https://doi.org/10.1002/qj.49708034504, 1954.

Becker, T. and Wing, A. A.: Understanding the Extreme Spread in Climate Sensitivity within the Radiative-Convective Equilibrium Model Intercomparison Project, Journal of Advances in Modeling Earth Systems, 12, e2020MS002 165, https://doi.org/https://doi.org/10.1029/2020MS002165, e2020MS002165 10.1029/2020MS002165, 2020.

Blyth, A. M.: Entrainment in Cumulus Clouds, Journal of Applied Meteorology and Climatology, 32, 626 – 641, https://doi.org/10.1175/1520-0450(1993)032<0626:EICC>2.0.CO;2, 1993.

Bony, S. and Dufresne, J.-L.: Marine boundary layer clouds at the heart of tropical cloud feedback uncertainties in climate models, Geophysical Research Letters, 32, https://doi.org/https://doi.org/10.1029/2005GL023851, 2005.

Bony, S. and SAFIRE: "MAESTRO-2024_SAFIRE-ATR42_SAFIRE_FAST Temperature and Humidity Fast Observation 25HZ", https://doi.org/10.25326/738, 2024.

Bony, S. and Stevens, B.: Measuring Area-Averaged Vertical Motions with Dropsondes, J. Atmos. Sci, 76, 767–783, 2019.

Bony, S., Stevens, B., Frierson, D. M. W., Jakob, C., Kageyama, M., Shepherd, R. P. T. G., Sherwood, S. C., Siebesma, A. P., Sobel, A. H., Watanabe, M., and Webb, M. J.: Clouds, circulation and climate sensitivity., Nature Geosci., 8, 261–268, https://doi.org/https://doi.org/10.1038/ngeo2398, 2015.

Bony, S., Stevens, B., Ament, F., Bigorre, S., Chazette, P., Crewell, S., Delanoë, J., Emanuel, K., Farrell, D., Flamant, C., Gross, S., Hirsch, L., Karstensen, J., Mayer, B., Nuijens, L., Ruppert Jr., J. H., Sandu, I., Siebesma, P., Speich, S., Szczap, F., Totems, J., Vogel, R., Wendisch, M., and Wirth, M.: EUREC$^4$A: A field campaign to elucidate the couplings between clouds, convection and circulation, Surveys in Geophysics, 38, 1529–1568, https://doi.org/10.1007/s10712-017-9428-0, 2017.

Bony, S., Schulz, H., Vial, J., and Stevens, B.: Sugar, Gravel, Fish, and Flowers: Dependence of Mesoscale Patterns of Trade-Wind Clouds on Environmental Conditions, Geophysical Research Letters, 47, e2019GL085 988, https://doi.org/https://doi.org/10.1029/2019GL085988, 2020.

Bony, S., Lothon, M., Delanoë, J., Coutris, P., Etienne, J.-C., Aemisegger, F., Albright, A. L., André, T., Bellec, H., Baron, A., Bourdinot, J.-F., Brilouet, P.-E., Bourdon, A., Canonici, J.-C., Caudoux, C., Chazette, P., Cluzeau, M., Cornet, C., Desbios, J.-P., Duchanoy, D., Flamant, C., Fildier, B., Gourbeyre, C., Guiraud, L., Jiang, T., Lainard, C., Le Gac, C., Lendroit, C., Lernould, J., Perrin, T., Pouvesle, F., Richard, P., Rochetin, N., Salaün, K., Schwarzenboeck, A., Seurat, G., Stevens, B., Totems, J., Touzé-Peiffer, L., Vergez, G., Vial, J., Villiger, L., and Vogel, R.: EUREC$^4$A observations from the SAFIRE ATR42 aircraft, Earth System Science Data Discussions, 2022, 1–61, https://doi.org/10.5194/essd-2021-459, 2022.

Brahimi, M. and Doan-Kim-Son: Interaction between two turbulent plumes in close proximity, Mechanics Research Communications, 12, 249–255, https://doi.org/https://doi.org/10.1016/0093-6413(85)90040-0, 1985.

Bretherton, C. S.: A Theory for Nonprecipitating Moist Convection between Two Parallel Plates. Part I: Thermodynamics and "Linear" Solutions, Journal of Atmospheric Sciences, 44, 1809 – 1827, https://doi.org/10.1175/1520-0469(1987)044<1809:ATFNMC>2.0.CO;2, 1987.

Bretherton, C. S. and Blossey, P. N.: Understanding Mesoscale Aggregation of Shallow Cumulus Convection Using Large-Eddy Simulation, Journal of Advances in Modeling Earth Systems, 9, 2798–2821, https://doi.org/https://doi.org/10.1002/2017MS000981, 2017.

Brient, F., Schneider, T., Tan, Z., Bony, S., Qu, X., and Hall, A.: Shallowness of tropical low clouds as a predictor of climate models' response to warming., Climate Dynamics, 47, 433–449, 2016.

Brilouet, P.-E., Lothon, M., Etienne, J.-C., Richard, P., Bony, S., Lernoult, J., Bellec, H., Vergez, G., Perrin, T., Delanoë, J., Jiang, T., Pouvesle, F., Lainard, C., Cluzeau, M., Guiraud, L., Medina, P., and Charoy, T.: The EUREC$^4$A turbulence dataset derived from the SAFIRE ATR 42 aircraft, Earth System Science Data, 13, 3379–3398, https://doi.org/10.5194/essd-13-3379-2021, 2021.

Byers, H. R. and Hall, R. K.: a Census of Cumulus-Cloud Height Versus Precipitation in the Vicinity of Puerto Rico during the Winter and Spring of 1953-1954., Journal of the Atmospheric Sciences, 12, 176–178, https://doi.org/10.1175/1520-0469(1955)012<0176:ACOCCH>2.0.CO;2, 1955.

Böing, S. J., Jonker, H. J. J., Siebesma, A. P., and Grabowski, W. W.: Influence of the Subcloud Layer on the Development of a Deep Convective Ensemble, Journal of the Atmospheric Sciences, 69, 2682 – 2698, https://doi.org/10.1175/JAS-D-11-0317.1, 2012.

Chandra, A. S., Kollias, P., and Albrecht, B. A.: Multiyear Summertime Observations of Daytime Fair-Weather Cumuli at the ARM Southern Great Plains Facility, Journal of Climate, 26, 10 031 – 10 050, https://doi.org/10.1175/JCLI-D-12-00223.1, 2013.

Chazette, P., Totems, J., Baron, A., Flamant, C., and Bony, S.: Trade-wind clouds and aerosols characterized by airborne horizontal lidar measurements during the EUREC$^4$A field campaign, Earth System Science Data, 12, 2919–2936, https://doi.org/10.5194/essd-12-2919-2020, 2020.

Cohen, B. G. and Craig, G. C.: Fluctuations in an Equilibrium Convective Ensemble. Part II: Numerical experiments., Journal of the Atmospheric Sciences, 63, 2005 – 2015, https://doi.org/10.1175/JAS3710.1, 2006.

Craig, G. C. and Cohen, B. G.: Fluctuations in an Equilibrium Convective Ensemble. Part I: Theoretical Formulation, Journal of the Atmospheric Sciences, 63, 1996 – 2004, https://doi.org/10.1175/JAS3709.1, 2006.

Dawe, J. T. and Austin, P. H.: Statistical analysis of an LES shallow cumulus cloud ensemble using a cloud tracking algorithm, Atmospheric Chemistry and Physics, 12, 1101–1119, https://doi.org/10.5194/acp-12-1101-2012, 2012.

Delanoë, J., Protat, A., Vinson, J.-P., Brett, W., Caudoux, C., Bertrand, F., Parent du Chatelet, J., Hallali, R., Barthes, L., Haeffelin, M., and Dupont, J.-C.: BASTA: A 95-GHz FMCW Doppler Radar for Cloud and Fog Studies, J. Atmos. Oceanic Technol., 33, 1023–1038, 2016.

Delanoë, J., Chazette, P., Bony, S., Totems, J., Flamant, C., and Baron, A.: SAFIRE ATR42: BASTALIAS L2 dataset, https://doi.org/10.25326/316, 2021.

George, G., Stevens, B., Bony, S., Pincus, R., Fairall, C., Schulz, H., Kölling, T., Kalen, Q. T., Klingebiel, M., Konow, H., Lundry, A., Prange, M., and Radtke, J.: JOANNE: Joint dropsonde Observations of the Atmosphere in tropical North atlaNtic meso-scale Environments, Earth System Science Data, 13, 5253–5272, https://doi.org/10.5194/essd-13-5253-2021, 2021.

George, G., Stevens, B., Bony, S., Vogel, R., and Naumann, A. K.: Widespread shallow mesoscale circulations observed in the trades, Nature Geoscience, 16, 584–589, https://doi.org/10.1038/s41561-023-01215-1, 2023.

Grabowski, W. W., Bechtold, P., Cheng, A., Forbes, R., Halliwell, C., Khairoutdinov, M., Lang, S., Nasuno, T., Petch, J., Tao, W.-K., Wong, R., Wu, X., and Xu, K.-M.: Daytime convective development over land: A model intercomparison based on LBA observations, Quarterly Journal of the Royal Meteorological Society, 132, 317–344, https://doi.org/https://doi.org/10.1256/qj.04.147, 2006.

Jaffeux, L. and Lothon, M.: MAESTRO 2024 Turbulence Dataset, https://doi.org/doi.org/10.25326/812, 2025.

Jaffeux, L., Lothon, M., Couvreux, F., Bouniol, D., Cayez, G., Joly, L., Burgalat, J., De Saint-Léger, C., Bellec, H., Henry, O., Chbib, D., Jiang, T., and Bony, S.: The MAESTRO turbulence dataset derived from the SAFIRE ATR42 aircraft, Earth System Science Data, essd-2025-586, submitted.

Janssens, M., Vilà-Guerau de Arellano, J., Scheffer, M., Antonissen, C., Siebesma, A. P., and Glassmeier, F.: Cloud Patterns in the Trades Have Four Interpretable Dimensions, Geophysical Research Letters, 48, e2020GL091 001, https://doi.org/https://doi.org/10.1029/2020GL091001, 2021.

Janssens, M., de Arellano, J. V.-G., van Heerwaarden, C. C., de Roode, S. R., Siebesma, A. P., and Glassmeier, F.: Nonprecipitating Shallow Cumulus Convection Is Intrinsically Unstable to Length Scale Growth, Journal of the Atmospheric Sciences, 80, 849 – 870, https://doi.org/10.1175/JAS-D-22-0111.1, 2023.

Janssens, M., George, G., Schulz, H., Couvreux, F., and Bouniol, D.: Shallow Convective Heating in Weak Temperature Gradient Balance Explains Mesoscale Vertical Motions in the Trades, Journal of Geophysical Research: Atmospheres, 129, e2024JD041 417, https://doi.org/https://doi.org/10.1029/2024JD041417, e2024JD041417 2024JD041417, 2024.

Jansson, F., Janssens, M., Grönqvist, J. H., Siebesma, A. P., Glassmeier, F., Attema, J., Azizi, V., Satoh, M., Sato, Y., Schulz, H., and Kölling, T.: Cloud Botany: Shallow Cumulus Clouds in an Ensemble of Idealized Large-Domain Large-Eddy Simulations of the Trades, Journal of Advances in Modeling Earth Systems, 15, e2023MS003 796, https://doi.org/https://doi.org/10.1029/2023MS003796, e2023MS003796 2023MS003796, 2023.

Joseph, J. H. and Cahalan, R. F.: Nearest Neighbor Spacing of Fair Weather Cumulus Clouds, Journal of Applied Meteorology (1988-2005), 29, 793–805, http://www.jstor.org/stable/26185140, 1990.

Kaye, N. B. and Linden, P. F.: Coalescing axisymmetric turbulent plumes, Journal of Fluid Mechanics, 502, 41–63, https://doi.org/10.1017/S0022112003007250, 2004.

Khairoutdinov, M. and Randall, D.: High-Resolution Simulation of Shallow-to-Deep Convection Transition over Land, Journal of the Atmospheric Sciences, 63, 3421 – 3436, https://doi.org/10.1175/JAS3810.1, 2006.

Konow, H., Ewald, F., George, G., Jacob, M., Klingebiel, M., Kölling, T., Luebke, A. E., Mieslinger, T., Pörtge, V., Radtke, J., Schäfer, M., Schulz, H., Vogel, R., Wirth, M., Bony, S., Crewell, S., Ehrlich, A., Forster, L., Giez, A., Gödde, F., Groß, S., Gutleben, M., Hagen, M., Hirsch, L., Jansen, F., Lang, T., Mayer, B., Mech, M., Prange, M., Schnitt, S., Vial, J., Walbröl, A., Wendisch, M., Wolf, K., Zinner, T., Zöger, M., Ament, F., and Stevens, B.: EUREC$^4$A's *HALO*, Earth System Science Data, 13, 5545–5563, https://doi.org/10.5194/essd-13-5545-2021, 2021.

Kuang, Z. and Bretherton, C. S.: A Mass-Flux Scheme View of a High-Resolution Simulation of a Transition from Shallow to Deep Cumulus Convection, Journal of the Atmospheric Sciences, 63, 1895 – 1909, https://doi.org/10.1175/JAS3723.1, 2006.

Lamer, K. and Kollias, P.: Observations of fair-weather cumuli over land: Dynamical factors controlling cloud size and cover, Geophysical Research Letters, 42, 8693–8701, https://doi.org/https://doi.org/10.1002/2015GL064534, 2015.

Lamer, K., Kollias, P., and Nuijens, L.: Observations of the variability of shallow trade wind cumulus cloudiness and mass flux, Journal of Geophysical Research: Atmospheres, 120, 6161–6178, https://doi.org/https://doi.org/10.1002/2014JD022950, 2015.

Lareau, N. P., Zhang, Y., and Klein, S. A.: Observed Boundary Layer Controls on Shallow Cumulus at the ARM Southern Great Plains Site, Journal of the Atmospheric Sciences, 75, 2235 – 2255, https://doi.org/10.1175/JAS-D-17-0244.1, 2018.

LeMone, M. A. and Pennell, W. T.: The relationship of trade-wind cumulus distribution to subcloud-layer fluxes and structure, Monthly Weather Review, 104, 524 – 539, https://doi.org/10.1175/1520-0493(1976)104<0524:TROTWC>2.0.CO;2, 1976.

LeMone, M. A. and Zipser, E. J.: Cumulonimbus Vertical Velocity Events in GATE. Part I: Diameter, Intensity and Mass Flux, Journal of Atmospheric Sciences, 37, 2444 – 2457, https://doi.org/10.1175/1520-0469(1980)037<2444:CVVEIG>2.0.CO;2, 1980.

Lenschow, D. and Stephens, P.: The role of thermals in the convective boundary layer, Boundary-Layer Meteorology, 19, 509–532, https://doi.org/10.1007/BF00122351, 1980.

Li, S., Chen, J., and Li, P.: MixtureInf: Inference for Finite Mixture Models, http://cran.r-project.org/package=MixtureInf, r package version 1.1, 2016.

Lothon, M. and Brilouet, P.-E.: SAFIRE ATR42: Turbulence Data 25 Hz (v1.9)., https://doi.org/10.25326/128, 2020.

López, R. E.: The Lognormal Distribution and Cumulus Cloud Populations, Monthly Weather Review, 105, 865 – 872, https://doi.org/10.1175/1520-0493(1977)105<0865:TLDACC>2.0.CO;2, 1977.

Malkus, J. S. and Ronne, C.: Concerning the Structure of Some Cumulus Clouds which Penetrated the High Tropical Troposphere, Tech. Rep. 27, Woods Hole Oceanographic Institution, 1954.

Maury, N., Rochetin, N., and Bony, S.: Interplay between convective structures and mesoscale circulation in a case of transition from scattered to aggregated marine shallow cumulus clouds., in preparation.

Mei, S.-J. and Yuan, C.: Three-dimensional simulation of building thermal plumes merging in calm conditions: Turbulence model evaluation and turbulence structure analysis, Building and Environment, 203, 108 097, https://doi.org/https://doi.org/10.1016/j.buildenv.2021.108097, 2021.

Miao, Q., Geerts, B., and LeMone, M.: Vertical Velocity and Buoyancy Characteristics of Coherent Echo Plumes in the Convective Boundary Layer, Detected by a Profiling Airborne Radar, Journal of Applied Meteorology and Climatology, 45, 838 – 855, https://doi.org/10.1175/JAM2375.1, 2006.

Mieslinger, T., Horváth, A., Buehler, S. A., and Sakradzija, M.: The Dependence of Shallow Cumulus Macrophysical Properties on Large-Scale Meteorology as Observed in ASTER Imagery, Journal of Geophysical Research, 124, 11 477–11 505, https://doi.org/https://doi.org/10.1029/2019JD030768, 2019.

Morrison, H., Peters, J. M., Chandrakar, K. K., and Sherwood, S. C.: Influences of Environmental Relative Humidity and Horizontal Scale of Subcloud Ascent on Deep Convective Initiation, Journal of the Atmospheric Sciences, 79, 337 – 359, https://doi.org/10.1175/JAS-D-21-0056.1, 2022.

Muller, C., Yang, D., Craig, G., Cronin, T., Fildier, B., Haerter, J. O., Hohenegger, C., Mapes, B., Randall, D., Shamekh, S., and Sherwood, S. C.: Spontaneous Aggregation of Convective Storms, Annual Review of Fluid Mechanics, 54, 133–157, https://doi.org/10.1146/annurev-fluid-022421-011319, 2022.

Narenpitak, P., Kazil, J., Yamaguchi, T., Quinn, P., and Feingold, G.: From Sugar to Flowers: A Transition of Shallow Cumulus Organization During ATOMIC, Journal of Advances in Modeling Earth Systems, 13, e2021MS002 619, https://doi.org/https://doi.org/10.1029/2021MS002619, 2021.

Neggers, R. A. J.: Exploring bin-macrophysics models for moist convective transport and clouds, Journal of Advances in Modeling Earth Systems, 7, 2079–2104, https://doi.org/https://doi.org/10.1002/2015MS000502, 2015.

Neggers, R. A. J. and Griewank, P. J.: A Decentralized Approach for Modeling Organized Convection Based on Thermal Populations on Microgrids, Journal of Advances in Modeling Earth Systems, 14, e2022MS003 042, https://doi.org/https://doi.org/10.1029/2022MS003042, 2022.

Neggers, R. A. J., Jonker, H. J. J., and Siebesma, A. P.: Size Statistics of Cumulus Cloud Populations in Large-Eddy Simulations, Journal of the Atmospheric Sciences, 60, 1060 – 1074, https://doi.org/10.1175/1520-0469(2003)60<1060:SSOCCP>2.0.CO;2, 2003.

Nuijens, L. and Siebesma, A. P.: Boundary Layer Clouds and Convection over Subtropical Oceans in our Current and in a Warmer Climate, Current Climate Change Reports, 5, 80–94, https://doi.org/10.1007/s40641-019-00126-x, 2019.

Nuijens, L., Serikov, I., Hirsch, L., Lonitz, K., and Stevens, B.: The distribution and variability of low-level cloud in the North Atlantic trades, Quarterly Journal of the Royal Meteorological Society, 140, 2364–2374, https://doi.org/https://doi.org/10.1002/qj.2307, 2014.

Ooyama, K.: Theory on parameterization of cumulus convection., Journal of the Meteorological Society of Japan, 49, 744 – 756, 1971.

Pera, L. and Gebhart, B.: Laminar plume interactions, Journal of Fluid Mechanics, 68, 259–271, https://doi.org/10.1017/S0022112075000791, 1975.

Poujol, B.: On the role of multiscale atmospheric circulations in the organization of tropical convection, Ph.D. thesis, Sorbonne University, 2025.

Rasp, S., Schulz, H., Bony, S., and Stevens, B.: Combining Crowdsourcing and Deep Learning to Explore the Mesoscale Organization of Shallow Convection, Bulletin of the American Meteorological Society, 101, E1980 – E1995, https://doi.org/10.1175/BAMS-D-19-0324.1, 2020.

Rauber, R. M., Stevens, B., Ochs, H. T., Knight, C., Albrecht, B. A., Blyth, A. M., Fairall, C. W., Jensen, J. B., Lasher-Trapp, S. G., Mayol-Bracero, O. L., Vali, G., Anderson, J. R., Baker, B. A., Bandy, A. R., Burnet, E., Brenguier, J.-L., Brewer, W. A., Brown, P. R. A., Chuang, R., Cotton, W. R., Girolamo, L. D., Geerts, B., Gerber, H., Göke, S., Gomes, L., Heikes, B. G., Hudson, J. G., Kollias, P., Lawson, R. R., Krueger, S. K., Lenschow, D. H., Nuijens, L., O'Sullivan, D. W., Rilling, R. A., Rogers, D. C., Siebesma, A. P., Snodgrass, E., Stith, J. L., Thornton, D. C., Tucker, S., Twohy, C. H., and Zuidema, P.: Rain in Shallow Cumulus Over the Ocean: The RICO Campaign, Bulletin of the American Meteorological Society, 88, 1912 – 1928, https://doi.org/10.1175/BAMS-88-12-1912, 2007.

Rochetin, N., Couvreux, F., Grandpeix, J.-Y., and Rio, C.: Deep Convection Triggering by Boundary Layer Thermals. Part I: LES Analysis and Stochastic Triggering Formulation, Journal of the Atmospheric Sciences, 71, 496 – 514, https://doi.org/10.1175/JAS-D-12-0336.1, 2014.

Rooney, G. G.: Merging of two or more plumes arranged around a circle, Journal of Fluid Mechanics, 796, 712–731, https://doi.org/10.1017/jfm.2016.272, 2016.

Rousseau-Rizzi, R., Kirshbaum, D. J., and Yau, M. K.: Initiation of Deep Convection over an Idealized Mesoscale Convergence Line, Journal of the Atmospheric Sciences, 74, 835 – 853, https://doi.org/10.1175/JAS-D-16-0221.1, 2017.

Sakradzija, M., Seifert, A., and Heus, T.: Fluctuations in a quasi-stationary shallow cumulus cloud ensemble, Nonlinear Processes in Geophysics, 22, 65–85, https://doi.org/10.5194/npg-22-65-2015, 2015.

Savre, J. and Craig, G.: Fitting Cumulus Cloud Size Distributions From Idealized Cloud Resolving Model Simulations, Journal of Advances in Modeling Earth Systems, 15, e2022MS003 360, https://doi.org/https://doi.org/10.1029/2022MS003360, e2022MS003360 2022MS003360, 2023.

Schulz, H.: C$^3$ONTEXT: a Common Consensus on Convective OrgaNizaTion during the EUREC$^4$A eXperimenT, Earth System Science Data, 14, 1233–1256, https://doi.org/10.5194/essd-14-1233-2022, 2022.

Schulz, H., Eastman, R., and Stevens, B.: Characterization and Evolution of Organized Shallow Convection in the Downstream North Atlantic Trades, Journal of Geophysical Research, 126, e2021JD034 575, https://doi.org/https://doi.org/10.1029/2021JD034575, 2021.

Seifert, A. and Heus, T.: Large-eddy simulation of organized precipitating trade wind cumulus clouds, Atmospheric Chemistry and Physics, 13, 5631–5645, https://doi.org/10.5194/acp-13-5631-2013, 2013.

Simpson, J., Simpson, R. H., Andrews, D. A., and Eaton, M. A.: Experimental cumulus dynamics, Reviews of Geophysics, 3, 387–431, https://doi.org/https://doi.org/10.1029/RG003i003p00387, 1965.

Simpson, J., Westcott, N., Clerman, R., and Pielke, R. A.: On cumulus mergers., Archiv für Meteorologie, Geophysik und Bioklimatologie, Serie A, 29, 1–40, https://doi.org/https://doi.org/10.1007/BF02247731, 1980.

Stevens, B., Bony, S., Brogniez, H., Hentgen, L., Hohenegger, C., Kiemle, C., L'Ecuyer, T. S., Naumann, A. K., Schulz, H., Siebesma, P. A., Vial, J., Winker, D. M., and Zuidema, P.: Sugar, gravel, fish and flowers: Mesoscale cloud patterns in the trade winds, Quarterly Journal of the Royal Meteorological Society, 146, 141–152, https://doi.org/https://doi.org/10.1002/qj.3662, 2020.

Stevens, B., Bony, S., Farrell, D., Ament, F., Blyth, A., Fairall, C., Karstensen, J., Quinn, P. K., Speich, S., Acquistapace, C., Aemisegger, F., Albright, A. L., Bellenger, H., Bodenschatz, E., Caesar, K.-A., Chewitt-Lucas, R., de Boer, G., Delanoë, J., Denby, L., Ewald, F., Fildier, B., Forde, M., George, G., Gross, S., Hagen, M., Hausold, A., Heywood, K. J., Hirsch, L., Jacob, M., Jansen, F., Kinne, S., Klocke, D., Kölling, T., Konow, H., Lothon, M., Mohr, W., Naumann, A. K., Nuijens, L., Olivier, L., Pincus, R., Pöhlker, M., Reverdin, G., Roberts, G., Schnitt, S., Schulz, H., Siebesma, A. P., Stephan, C. C., Sullivan, P., Touzé-Peiffer, L., Vial, J., Vogel, R., Zuidema, P., Alexander, N., Alves, L., Arixi, S., Asmath, H., Bagheri, G., Baier, K., Bailey, A., Baranowski, D., Baron, A., Barrau, S., Barrett, P. A., Batier, F., Behrendt, A., Bendinger, A., Beucher, F., Bigorre, S., Blades, E., Blossey, P., Bock, O., Böing, S., Bosser, P., Bourras, D., Bouruet-Aubertot, P., Bower, K., Branellec, P., Branger, H., Brennek, M., Brewer, A., Brilouet, P.-E., Brügmann, B., Buehler, S. A., Burke, E., Burton, R., Calmer, R., Canonici, J.-C., Carton, X., Cato Jr., G., Charles, J. A., Chazette, P., Chen, Y., Chilinski, M. T., Choularton, T., Chuang, P., Clarke, S., Coe, H., Cornet, C., Coutris, P., Couvreux, F., Crewell, S., Cronin, T., Cui, Z., Cuypers, Y., Daley, A., Damerell, G. M., Dauhut, T., Deneke, H., Desbios, J.-P., Dörner, S., Donner, S., Douet, V., Drushka, K., Dütsch, M., Ehrlich, A., Emanuel, K., Emmanouilidis, A., Etienne, J.-C., Etienne-Leblanc, S., Faure, G., Feingold, G., Ferrero, L., Fix, A., Flamant, C., Flatau, P. J., Foltz, G. R., Forster, L., Furtuna, I., Gadian, A., Galewsky, J., Gallagher, M., Gallimore, P., Gaston, C., Gentemann, C., Geyskens, N., Giez, A., Gollop, J., Gouirand, I., Gourbeyre, C., de Graaf, D., de Groot, G. E., Grosz, R., Güttler, J., Gutleben, M., Hall, K., Harris, G., Helfer, K. C., Henze, D., Herbert, C., Holanda, B., Ibanez-Landeta, A., Intrieri, J., Iyer, S., Julien, F., Kalesse, H., Kazil, J., Kellman, A., Kidane, A. T., Kirchner, U., Klingebiel, M., Körner, M., Kremper, L. A., Kretzschmar, J., Krüger, O., Kumala, W., Kurz, A., L'Hégaret, P., Labaste, M., Lachlan-Cope, T., Laing, A., Landschützer, P., Lang, T., Lange, D., Lange, I., Laplace, C., Lavik, G., Laxenaire, R., Le Bihan, C., Leandro, M., Lefevre, N., Lena, M., Lenschow, D., Li, Q., Lloyd, G., Los, S., Losi, N., Lovell, O., Luneau, C., Makuch, P., Malinowski, S., Manta, G., Marinou, E., Marsden, N., Masson, S., Maury, N., Mayer, B., Mayers-Als, M., Mazel, C., McGeary, W., McWilliams, J. C., Mech, M., Mehlmann, M., Meroni, A. N., Mieslinger, T., Minikin, A., Minnett, P., Möller, G., Morfa Avalos, Y., Muller, C., Musat, I., Napoli, A., Neuberger, A., Noisel, C., Noone, D., Nordsiek, F., Nowak, J. L., Oswald, L., Parker, D. J., Peck, C., Person, R., Philippi, M., Plueddemann, A., Pöhlker, C., Pörtge, V., Pöschl, U., Pologne, L., Posyniak, M., Prange, M., Quiñones Meléndez, E., Radtke, J., Ramage,

K., Reimann, J., Renault, L., Reus, K., Reyes, A., Ribbe, J., Ringel, M., Ritschel, M., Rocha, C. B., Rochetin, N., Röttenbacher, J., Rollo, C., Royer, H., Sadoulet, P., Saffin, L., Sandiford, S., Sandu, I., Schäfer, M., Schemann, V., Schirmacher, I., Schlenczek, O., Schmidt, J., Schröder, M., Schwarzenboeck, A., Sealy, A., Senff, C. J., Serikov, I., Shohan, S., Siddle, E., Smirnov, A., Späth, F., Spooner, B., Stolla, M. K., Szkółka, W., de Szoeke, S. P., Tarot, S., Tetoni, E., Thompson, E., Thomson, J., Tomassini, L., Totems, J., Ubele, A. A., Villiger, L., von Arx, J., Wagner, T., Walther, A., Webber, B., Wendisch, M., Whitehall, S., Wiltshire, A., Wing, A. A., Wirth, M., Wiskandt, J., Wolf, K., Worbes, L., Wright, E., Wulfmeyer, V., Young, S., Zhang, C., Zhang, D., Ziemen, F., Zinner, T., and Zöger, M.: EUREC$^4$A, Earth System Science Data, 13, 4067–4119, https://doi.org/10.5194/essd-13-4067-2021, 2021.

Touzé-Peiffer, L., Vogel, R., and Rochetin, N.: Cold Pools Observed during EUREC4A: Detection and Characterization from Atmospheric Soundings, Journal of Applied Meteorology and Climatology, 61, 593 – 610, https://doi.org/10.1175/JAMC-D-21-0048.1, 2022.

Vial, J., Bony, S., Stevens, B., and Vogel, R.: Mechanisms and Model Diversity of Trade-Wind Shallow Cumulus Cloud Feedbacks: A Review., Survey of Geophys., 38, 1331–1353, https://doi.org/https://doi.org/10.1007/s10712-017-9418-2, 2017.

Vial, J., Vogel, R., and Schulz, H.: On the daily cycle of mesoscale cloud organization in the winter trades, Quarterly Journal of the Royal Meteorological Society, 147, 2850–2873, https://doi.org/https://doi.org/10.1002/qj.4103, 2021.

Vial, J., Albright, A. L., Vogel, R., Musat, I., and Bony, S.: Cloud transition across the daily cycle illuminates model responses of trade cumuli to warming, Proceedings of the National Academy of Sciences, 120, e2209805 120, https://doi.org/10.1073/pnas.2209805120, 2023.

Vogel, R., Bony, S., and Stevens, B.: Estimating the Shallow Convective Mass Flux from the Subcloud-Layer Mass Budget, Journal of the Atmospheric Sciences, 77, 1559 – 1574, https://doi.org/10.1175/JAS-D-19-0135.1, 2020.

Vogel, R., Albright, A. L., Vial, J., George, G., Stevens, B., and Bony, S.: Strong cloud–circulation coupling explains weak trade cumulus feedback, Nature, 612, 696–700, https://doi.org/10.1038/s41586-022-05364-y, 2022.

Williams, A. and Hacker, J.: Interactions between coherent eddies in the lower convective boundary layer, Boundary-Layer Meteorology, 64, 55–74, https://doi.org/10.1007/BF00705662, 1993.

Öktem, R. and Romps, D. M.: Prediction for Cloud Spacing Confirmed Using Stereo Cameras, Journal of the Atmospheric Sciences, 78, 3717 – 3725, https://doi.org/10.1175/JAS-D-21-0026.1, 2021.